The Astrophysical Journal, 966:80 (25pp), 2024 May 1 https://doi.org/10.3847/1538-4357/ad307b

METAL-Z: Measuring Dust Depletion in Low-metallicity Dwarf Galaxies

Aleksandra Hamanowicz[1], Kirill Tchernyshyov[2], Julia Roman-Duval[1], Edward B. Jenkins[3], Marc Rafelski[1], Karl D. Gordon[1], Yong Zheng[4], Miriam Garcia[5], and Jessica Werk[2]
[1] Space Telescope Science Institute, 3700 San Martin Drive, Baltimore, MD 21218, USA; ahamanowicz@stsci.edu
[2] Department of Astronomy, Box 351580, University of Washington, Seattle, WA 98195, USA
[3] Department of Astrophysical Sciences, Princeton University, Princeton, NJ 08544-1001, USA
[4] Department of Physics, Applied Physics, and Astronomy, Rensselaer Polytechnic Institute, 110 8th Street, Troy, NY 12180, USA
[5] Centro de Astrobiologia, CSIC-INTA, Dpto. de Astrofisica, Instituto Nacional de Tecnica Aeroespacial, Ctra. de Torrejon a Ajalvir, km 4, 28850 Torrejon de Ardoz Madrid, Spain
Received 2023 November 3; revised 2024 February 21; accepted 2024 February 23; published 2024 April 26

Abstract

The cycling of metals between interstellar gas and dust is a critical aspect of the baryon cycle of galaxies, yet our understanding of this process is limited. This study focuses on understanding dust depletion effects in the low-metallicity regime (<20% $Z_{\odot}$) typical of cosmic noon. Using medium-resolution UV spectroscopy from the Cosmic Origins Spectrograph on board the Hubble Space Telescope, gas-phase abundances and depletions of iron and sulfur were derived toward 18 sight lines in local dwarf galaxies IC 1613 and Sextans A. The results show that the depletion of Fe and S is consistent with that found in the Milky Way (MW), LMC, and SMC. The depletion level of Fe increases with gas column density, indicating dust growth in the interstellar medium. The level of Fe depletion decreases with decreasing metallicity, resulting in the fraction of iron in gas ranging from 3% in the MW to 9% in IC 1613 and ∼19% in Sextans A. The dust-to-gas and dust-to-metal ratios (D/G, D/M) for these dwarf galaxies were estimated based on the MW relations between the depletion of Fe and other elements. The study finds that D/G decreases only slightly sublinearly with metallicity, with D/M decreasing from 0.41 ± 0.05 in the MW to 0.11 ± 0.11 at 0.10 $Z_{\odot}$ (at $\log N(\mathrm{H}) = 21\ \mathrm{cm}^{-2}$). The trend of D/G versus metallicity using depletion in local systems is similar to that inferred in Damped Lyα systems from abundance ratios but lies higher than the trend inferred from far-IR measurements in nearby galaxies.

Unified Astronomy Thesaurus concepts: Interstellar medium (847); Interstellar dust processes (838); Galaxy chemical evolution (580); Gas-to-dust ratio (638); Interstellar abundances (832); Interstellar absorption (831); Interstellar line absorption (843)

Supporting material: machine-readable table

1. Introduction

Despite amounting to only a small fraction of the interstellar medium (ISM) mass, metals play a significant role in the evolution of galaxies. Formed in stellar interiors and explosions, metals gradually enrich the ISM and influence galaxies' properties and evolution through their effects on heating and cooling, radiative transfer, and chemistry. In particular, interstellar dust, the main constituents of which are carbon, oxygen, silicon, magnesium, and iron, absorbs stellar radiation in the optical and UV and reemits it in the far-IR (FIR), affecting the galaxies' spectral energy distribution (SED). The opacity of dust versus wavelength, in turn, depends on the composition and size of dust grains (e.g., Gordon et al. 2003; Demyk et al. 2017a, 2017c; Ysard et al. 2018). As a result, we need to understand the dust abundance and properties to correctly "de-redden" galaxy SEDs, infer their star formation histories and stellar populations, as well as to convert FIR emission into dust and gas masses, a common and very effective way to trace the ISM at all redshifts (Hildebrand 1983; Bolatto et al. 2011; Eales et al. 2012; Rowlands et al. 2012; Schruba et al. 2012; Rowlands et al. 2014).

The abundance of dust and the fraction of metals locked onto dust grains are described by the dust-to-gas (D/G) and dust-to-metal (D/M) ratios ($D/G = D/M \times \mathrm{Z}$, where Z is the metallicity of the system). These parameters are expected to vary with environment, especially with metallicity and density (Zhukovska et al. 2016). At low metallicity, fewer metals and dust grains are available, which means their collisions are rarer. As a result, the timescale for ISM dust growth is expected to be inversely proportional to metallicity, and, similarly, to gas density (Asano et al. 2013; Feldmann 2015; Zhukovska et al. 2016).

The dust-to-gas ratio can be measured through two methods. The most common and efficient approach is to measure the dust mass (or surface density for resolved observations) of galaxies through their FIR dust emission, and their gas mass (or surface density) through 21 cm to trace the atomic gas, and the CO rotational emission to estimate the molecular gas content (Rémy-Ruyer et al. 2014; De Vis et al. 2019). However, the conversion of FIR flux to dust mass relies on modeling. While the dust temperature can be estimated through multiband FIR photometry, the approach still relies on a purely theoretical estimate of the FIR opacity, which is known to vary with dust composition, shape, and size, and is observationally very poorly constrained (Stepnik et al. 2003; Demyk et al. 2017b; Clark et al. 2019). In turn, gas mass estimates suffer from uncertainties due to CO-dark gas and optically thick HI (Roman-Duval et al. 2014).

Table 1
Spectroscopic Targets and Their Stellar Parameters

Target	SIMBAD Resolved Name	R.A. (hr)	Decl. (deg)	SpT	V (mag)	$E(B-V)$[b] (mag)
IC1613-61331	[GHV2009] Star 61331	01:05:00.200	+02:09:13.10	O9.7 II	19.14	0.05
IC1613-62024	[GHV2009] Star 62024	01:05:00.646	+02:08:49.26	O6.5 IIIf	19.60	0.11
IC1613-64066	[GHV2009] Star 64066	01:05:20.700	+02:09:28.10	O3 III((f))	19.03	0.07
IC1613-67559	[GHV2009] Star 67559	01:05:04.767	+02:09:23.19	O8.5 III((f))	19.24	0.07
IC1613-67684	[GHV2009] Star 67684	01:05:04.900	+02:09:32.60	O8.5 I	19.02	0.05
IC1613-A13[a]	[BUG2007] A 13	01:05:06.250	+02:10:43.00	O3-4 V((f))	18.96	0.05
IC1613-B11[a]	[BUG2007] B 11	01:04:43.800	+02:06:44.75	O9.5 I	18.62	0.13
IC1613-B2	[BUG2007] B 2	01:05:03.068	+02:10:04.54	O7.5 III-V((f))	19.62	0.07
IC1613-B3	[BUG2007] B 3	01:05:06.370	+02:09:31.34	B0 Ia	17.69	0.10
IC1613-B7	[BUG2007] B 7	01:05:01.970	+02:08:05.10	O9 II	18.96	0.05
SEXTANS-A-s050	LGGS J101100.66-044044.3	10:11:00.660	−04:40:44.30	O9.7 I	19.61	0.01
SEXTANS-A-s014	LGGS J101053.81-044113.0	10:10:53.800	−04:41:13.00	O7.5 III((f))	20.69	0.01
SEXTANS-A-s022	[VPW98] 451	10:11:05.380	−04:42:40.10	O8 V	19.46	0.01
SEXTANS-A-s038	LGGS J101106.05-044211.4	10:11:06.047	−04:42:11.37	O9.7 I((f))	19.49	0.03
SEXTANS-A-s029[a]	[VPW98] 1744	10:10:58.190	−04:43:18.40	O8.5 III	20.80	0.02
SEXTANS-A-s037[a]	LGGS J101104.78-044224.1	10:11:04.770	−04:42:24.24	O9 I	20.68	0.03
SEXTANS-A-SA2[a]	LGGS J101056.86-044040.8	10:10:56.845	−04:40:40.90	O	20.41	0.00
SEXTANS-A-s021[a]	LGGS J101104.79-044220.9	10:11:04.790	−04:42:20.96	O8 V	20.60	−0.20

Notes. Names of stars in Sextans A are from Lorenzo et al. (2022), except for Sextans A SA2, which is not included in that catalog.
References: The SpT (spectral type) and V magnitudes of stars come from: Bresolin et al. (2007), Garcia et al. (2009), Garcia & Herrero (2013), and Garcia et al. (2014) for IC1613; Camacho et al. (2016), Lorenzo et al. (2022) for Sextans A.
[a] Sight lines with archival data.
[b] $E(B-V)$ reddening from the ULLYSES program.

The other method to estimate D/G and D/G in galaxies relies on UV spectroscopy of interstellar absorption lines to measure gas-phase abundances and depletions. The depletion of a given element X (e.g., Fe, Si, Mg, etc.) corresponds to the logarithm of the fraction of that element in the gas phase, and is expressed as follows:

$$\delta(\mathrm{X}) = \log_{10}(\mathrm{X/H})_{\mathrm{gas}} - \log_{10}(\mathrm{X/H})_{\mathrm{total}}, \quad (1)$$

where $\log_{10}(\mathrm{X/H})_{\mathrm{gas}}$ is the abundance of element X in the gas phase, and $\log_{10}(\mathrm{X/H})_{\mathrm{total}}$ is the total abundance of element X (in gas and dust). In the Milky Way (MW) and nearby galaxies, gas-phase abundances are measured through interstellar UV absorption lines toward UV-bright O and B stars. Total elemental abundances in the ISM are assumed to equal the photospheric abundances of young stars that recently formed out of interstellar gas and dust (Jenkins 2009). By summing the depletions of all major constituents of dust, one can estimate D/G and D/M (e.g., Roman-Duval et al. 2022a).

Understanding how depletions vary with environment (e.g., metallicity, gas density) is key to measuring the chemical enrichment of the Universe through Damped Lyα systems (DLAs; e.g., Rafelski et al. 2012; De Cia et al. 2016). DLAs are quasar absorbers with high hydrogen column density ($\log N(\mathrm{H\,I}) > 20.3\,\mathrm{cm}^{-2}$), and their detectability depends solely on the brightness of the background object. This makes DLAs a powerful tool for tracing the chemical enrichment of the Universe over the past nine billion years ($z < 5.3$). However, to infer the total metallicities from gas-phase metallicities in DLAs, it is necessary to correct the measurements for depletion effects, particularly for refractory elements such as Fe. Given that stellar abundances cannot be used as a proxy for total ISM abundances in those systems, depletion corrections are estimated from abundance ratios such as [S/Fe] or [Zn/Fe] tied to the calibration of Zn depletion versus [Zn/Fe] in the MW (De Cia et al. 2016). Such depletion corrections have only been compared to and calibrated against depletion measurements based on the comparison of gas-phase and stellar abundances in the MW, LMC, and Small Magellanic Cloud (SMC), down to 20% solar metallicity (Roman-Duval et al. 2022b), but depletion measurements in nearby galaxies of lower metallicities are still lacking.

Indeed, while we have a good understanding of the depletion rate of gas-phase metals in the MW (Jenkins 2009), depletion measurements remain sparse in low-metallicity environments ($Z < 20\%$ solar) because the observations, which require deep medium–high-resolution UV spectroscopy, are challenging. Relatively large samples of depletion measurements for some key constituents of dust (Fe, Mg, Si, Ni, Cr) and volatile elements (S, Zn) have recently been obtained in the LMC at 50% solar metallicity (Tchernyshyov et al. 2015; Roman-Duval et al. 2021) and SMC at 20% solar metallicity (Tchernyshyov et al. 2015; Jenkins & Wallerstein 2017). These studies have shown that the metals are more depleted as the gas density and metallicity increases, resulting in variations of the dust-to-metal (D/M) and dust-to-gas (D/G) ratios with both gas density and metallicity (Roman-Duval et al. 2022a). However, there have been no depletion measurements of this kind (i.e., toward individual stars in nearby galaxies) at metallicities lower than 20% solar to date.

Yet, depletion measurements from UV spectroscopy can provide estimates of the D/G, D/M, and dust composition, and offer a valuable tool for investigating the complex relationship between metallicity, gas density, and dust content in the ISM. In particular, a tension between FIR-based and depletion-based estimates of D/G and D/M has arisen in recent years. For galaxies with metallicities at or less than 20% solar, D/G measured through FIR emission is much lower than D/G

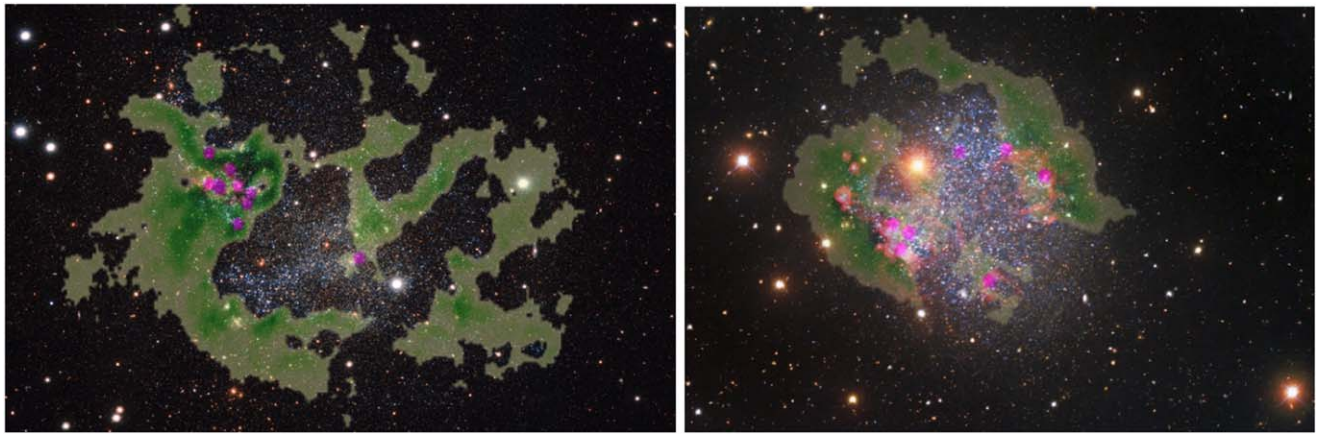

Figure 1. Visible images of IC 1613 (left) and Sextans A (right) showing the targets used in this study as magenta stars, and the HI 21 cm integrated intensity from LITTLE THINGS as the green transparent color scale. The image of IC 1613 is from OmegaCam on ESO's Very Large Telescope (credit: ESO), and the image of Sextans A is from the Nicholas U. Mayall 4 m Telescope at Kitt Peak National Observatory (credit: KPNO/NOIRLab/NSF/AURA data obtained and processed by P. Massey from Lowell Obs., G. Jacoby, K. Olsen, and C. Smith from AURA/NSF; image processing: T.A. Rector from University of Alaska Anchorage/NSF's NOIRLab, M. Zamani from NSF's NOIRLab, and D. de Martin from NSF's NOIRLab).

Table 2
Targets and Observations with COS/HST, Including Archival Data Sets

Target	Grating/Cenwave	LP[a]	T_{exp} (s)	PID[b]
IC1613-61331	G130M/1291	LP4	9000	GO-15880
IC1613-61331	G130M/1309	LP3	2900	GO-15880
IC1613-62024	G130M/1291	LP4	29,904	GO-15880
IC1613-62024	G130M/1309	LP3	4800	GO-15880
IC1613-64066	G130M/1291	LP4	4545	GO-15880
IC1613-64066	G130M/1309	LP3	3177	GO-15880
IC1613-67559	G130M/1291	LP4	11,845	GO-15880
IC1613-67559	G130M/1309	LP3	2419	GO-15880
IC1613-67684	G130M/1291	LP4	6900	GO-15880
IC1613-67684	G130M/1309	LP3	2200	GO-15880
IC1613-A13	G130M/1291	LP4	1680	GO-15880
IC1613-A13	G130M/1291	LP1	1911	GO-12867
IC1613-A13	G130M/1327	LP1	2729	GO-12867
IC1613-B11	G130M/1291	LP4	4210	GO-15880
IC1613-B11	G130M/1291	LP1	1852	GO-12867
IC1613-B11	G130M/1327	LP1	2729	GO-12867
IC1613-B2	G130M/1291	LP4	3123	GO-15880
IC1613-B3	G130M/1291	LP4	13,150	GO-15880
IC1613-B3	G130M/1309	LP3	6150	GO-15880
IC1613-B7	G130M/1291	LP4	18,650	GO-15156
SEXTANS-A-s050	G130M/1291	LP4	17,150	GO-15880
SEXTANS-A-s050	G130M/1309	LP3	8140	GO-15880
SEXTANS-A-s014	G130M/1291	LP4	22,240	GO-15880
SEXTANS-A-s014	G130M/1309	LP3	9840	GO-15880
SEXTANS-A-s022	G130M/1291	LP4	14,239	GO-15880
SEXTANS-A-s022	G130M/1309	LP3	4836	GO-15880
SEXTANS-A-s038	G130M/1291	LP4	14,582	GO-15880
SEXTANS-A-s038	G130M/1309	LP3	4836	GO-15880
SEXTANS-A-s029	G130M/1291	LP4	10,726	GO-15967
SEXTANS-A-s037	G130M/1291	LP4	12,846	GO-16767
SEXTANS-A-SA2	G130M/1291	LP4	10,180	GO-16767
SEXTANS-A-s021	G130M/1291	LP5	10,184	GO-16920

Notes.
[a] COS lifetime positions used for observations.
[b] Proposal ID corresponding to the observations.

derived from rest-frame UV spectroscopy in DLAs (Galliano et al. 2018; Roman-Duval et al. 2022a, 2022b; Popping & Péroux 2022). To understand dust properties and abundance below 20% solar metallicity and resolve this tension, we need to measure gas-phase abundances, elemental depletions, and, subsequently, D/G and D/M in nearby low-metallicity systems where stellar and gas-phase abundances can be measured and compared.

In this work, we present the "Metal Evolution, Transport, and Abundance at Low Metallicity (Z)" (METAL-Z) large program with the Hubble Space Telescope (HST; 77 orbits, GO-15880), designed to measure the gas-phase abundance and depletions of iron and sulfur (Fe and S), and infer D/G as a function of metallicity down to 0.1 $Z_{\odot}$. The program comprises medium-resolution UV spectra obtained with the Cosmic Origins Spectrograph (COS) on board the HST toward 14 massive O and early B stars in two local galaxies with metallicity $<$ 20% solar: IC 1613 (10% solar metallicity in oxygen, 20% solar metallicity in iron, distance 730 kpc) and Sextans A (10% solar metallicity, distance 1.3 Mpc).

This paper is organized as follows. In Section 2, we present the survey design and data reduction. Section 3 describes the derivation of column densities of hydrogen, iron, and sulfur. Section 4 examines the variations of the S and Fe depletions with gas density and metallicity. In Section 5, we present the derivation of D/G based on the depletion measurements in IC 1613 and Sextans A, combined with prior knowledge of depletion patterns obtained in the MW and Magellanic Clouds. Section 6 provides a summary of this work.

2. Survey Design

Measuring interstellar gas-phase abundances requires medium-resolution UV spectroscopy of bright background massive stars of type B0 or earlier (stars later than B0 have complex stellar continua with many weak lines unsuitable for ISM abundance determinations). Keeping the exposure time reasonable restricts the target pool to low-metallicity galaxies within ∼1.5 Mpc. The METAL-Z (GO-15880) large program with

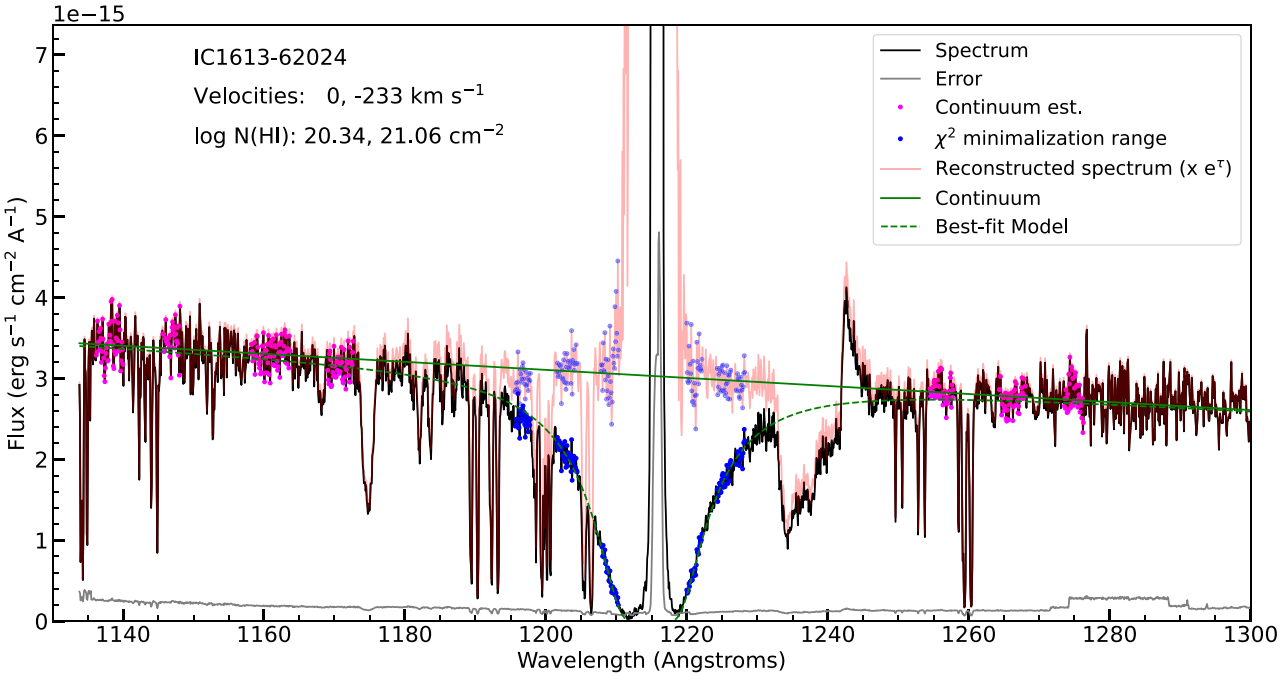

Figure 2. Illustration of the Lyα absorption line profile fitting procedure for sight line IC1613-62024. The spectrum is zoomed at ±80 Å around the rest-frame Lyα λ1216 Å line. Error per wavelength is shown in gray. The central Lyα absorption feature comes from the Milky Way and is blended with Lyα from the targeted galaxy (here, IC1613). In black, we show the smoothed data; blue points mark the regions included in the profile fit, while magenta points mark the continuum fit windows. Continuum fit is marked with a straight green line, and the fitted line profile is marked with a green dashed line. For reference, we also show the reconstructed spectrum in red. In the top left, we show best-fit model parameters: heliocentric velocities of the centers of the line components and corresponding H I column densities. Thanks to the significant velocity difference between Milky Way and METAL-Z galaxies, we can disentangle their H I profiles from the line asymmetry.

HST/COS observed several massive stars ($V < 19.5$) in IC 1613 ($12 + \log \mathrm{O/H} = 7.86$, or 13% solar Skillman et al. 1989) and Sextans A ($12 + \log \mathrm{O/H} = 7.54$, or 7% solar Kniazev et al. 2005). Those data are supplemented with archival observations of seven O and early B stars in Sextans A and IC 1613.

2.1. Target Sample

The sample is comprised of massive stars with spectral type B0 and earlier and with $V < 19.5$ mag, taken from OB star catalogs in IC 1613 (Bresolin et al. 2007; Garcia et al. 2014) and Sextans A (Camacho et al. 2016). All targets are listed in Table 1. O and early B stars have rotational velocities in excess of $\sim$70 km s^{-1} (Garcia et al. 2014; Tramper et al. 2014), minimizing the risk of confusion between ISM and stellar photospheric absorption lines. Indeed, the typical velocity dispersion in ISM is 10–20 km s^{-1} (Tamburro et al. 2009; Choudhuri & Roy 2019).

Most targets were observed under Hubble program GO-15880 (PI: Roman-Duval). Additionally, we supplemented the GO-15880 sample with the spectra of stars available in the archive: A13, B11, and B7 in IC 1613 (GO-12867, GO-15156) and s3, SA1, SA2, SA3 in Sextans A (GO-15967, GO-16920, and GO-16767). Note that the brightness of Sextans A star s3 falls below the original threshold $V < 19.5$ mag; however, due to a limited number of available stars in that galaxy and the availability of archival observations, we decided to include it.

Both galaxies (IC 1613, Sextans A) have high-resolution ($\sim$8″) Very Large Array (VLA) 21 cm data taken as part of the LITTLE THINGS (Hunter et al. 2012) or VLA-ANGST (Ott et al. 2012) surveys, providing spatially resolved information about the environment of the selected stellar sources and the estimates of the local N(H I) values.

The target sample is shown in Figure 1 for IC 1613 and Sextans A, along with H I 21 cm intensities from LITTLE THINGS and visible images of those galaxies from OmegaCam on ESO's Very Large Telescope and Nicholas U. Mayall 4 m Telescope at Kitt Peak National Observatory, respectively.

2.2. Observations: COS Spectroscopy

The COS spectra were obtained with the G130M grating, with some sight lines having the benefit of additional archival COS G160M observations. All observations are summarized in Table 2.

Hydrogen column density measurements are needed to derive abundances and depletion. The H I column density is typically measured using the Lyα (λ1216 Å) line. At the time of the survey design, it was unclear whether Lyα could be observed at LP4 given the COS2025 restrictions (Lyα falls in the gain-sag detector gap of G130M/1291). Therefore, Lyα was observed with the G130M/1309 at LP3, which was not impacted by gain-sag at the time of the observations.

We used the G130M/1291 setting of COS/far-UV (FUV) at LP4 (FP-POS 3 and 4) to cover the interstellar absorption lines from S and Fe: Fe II $\lambda\lambda\lambda$ 1142, 1143, 1144 Å and S II $\lambda\lambda\lambda$ 1250, 1253, 1259 Å. In addition, the 1291 spectra cover Si (Si II $\lambda\lambda\lambda\lambda$ 1190, 1193, 1260, 1304 Å), C (C II λ1334 Å), and O (O I λ1302 Å) lines. Those lines are strongly saturated and as such not usable for abundance measurements using standard techniques. The Mg II lines (Mg II $\lambda\lambda$ 1239, 1240 Å) are also covered in the 1291 spectra but not detected in any sight line except for IC 1613-62024.

Table 3
Central Wavelength and Oscillator Strength of Spectral Lines Used for Depletion Measurements

Element/Ion	Wavelength (Å)	$\log \lambda f_\lambda$ (Å)
S II	1250.578	0.809
	1253.805	1.113
	1259.518	1.295
Fe II	1142.366	0.661
	1143.226	1.342
	1144.938	1.978
	1608.451	1.968

References: The line strengths come from Kisielius et al. (2014) for S II and Morton (2003) for Fe II.

The observations targeted signal-to-noise ratio (S/N) = 15 with COS G130M/1291 to detect equivalent widths $W_\lambda > 50$ mÅ at 10σ, which is expected for the metallicity and N(H) of the sample. We used spectral dithering with two FP-POS positions (3 and 4) to mitigate the effects of the fixed pattern noise on the effective S/N. In the case of the targets with archival COS/FUV observations (see Table 1 inputs marked with *a*), we had to make sure that the S/N of the archival data were sufficient to conduct the hydrogen, S, and Fe column density measurements. As the S/N of the archival observations of the B11 and A13 stars in IC 1613 was not satisfactory, additional exposures with G130M/1291 were taken as part of METAL-Z/GO-15880.

2.3. Data Reduction

The COS spectra were retrieved from the MAST archive and processed with version 3.3.10 of the COS calibration pipeline, CalCOS. The different exposures for a given target were observed to be well aligned in wavelength, and no extra wavelength alignment was necessary.

The different spectra obtained for a given target were coadded using the following approach. First, the *x1d* spectra were resampled using the nearest neighbor interpolation on a common wavelength grid. This method avoids covariance and correlated errors between pixels. The wavelength grid is set to encompass the wavelength coverage of all the input exposures, with the coarsest dispersion among the input exposures (note that all spectra used in this work have comparable spectral resolution). For each wavelength sample, the coadded flux and errors are computed by performing the weighted sum of all the input fluxes, where the weight is set to the product of the sensitivity (net counts/flux) and exposure time. This weight provides an unbiased and noiseless estimate of the number of counts expected to fall in a given wavelength bin and is superior to a weighting scheme based on inverse squared errors because COS errors are asymmetric, particularly in the low count regime (COS Instrument Science Report 2021-03, Johnson et al. 2021). As a result, with an error-based weighting scheme, fluxes in noise troughs would be weighted higher than fluxes in noise peaks, resulting in a negative bias of the coadded fluxes. This bias can exceed 10% in the low count regime.

In addition to calculating coadded fluxes, the gross counts, background count rates, and flat-field-corrected sensitivities multiplied by exposure times were summed over the wavelength-interpolated *x1d* spectra. These values are stored to allow the use of a Poisson likelihood function when comparing spectrum models to the data. The motivation for not using the commonly adopted Gaussian approximation for spectrum uncertainties is the low S/N of some of the data, which leads to as few as ≈10 photons per pixel. The Poisson likelihood function is described in Section 3.3.1.

Table 4
Gas Column Density Measurements for IC 1613/Sextans A and the Milky Way, as Described in Section 3.1

Target	$\log N(\mathrm{H\,I})_{\mathrm{gal}}$[a] ($\mathrm{cm^{-2}}$)	$\log N(\mathrm{H\,I})_{\mathrm{MW}}$[b] ($\mathrm{cm^{-2}}$)
IC1613-61331	20.84 ± 0.02	20.11 ± 0.12
IC1613-62024	21.05 ± 0.03	20.39 ± 0.12
IC1613-64066	20.88 ± 0.03	20.34 ± 0.11
IC1613-67559	20.47 ± 0.09	20.42 ± 0.14
IC1613-67684	20.44 ± 0.03	20.23 ± 0.07
IC1613-A13	20.26 ± 0.03	20.29 ± 0.03
IC1613-B11	20.37 ± 0.03	20.22 ± 0.06
IC1613-B2	21.17 ± 0.03	20.35 ± 0.15
IC1613-B3	20.64 ± 0.05	20.23 ± 0.14
IC1613-B7	20.73 ± 0.04	20.37 ± 0.06
SEXTANS-A-s050	20.46 ± 0.04	20.61 ± 0.03
SEXTANS-A-s014	20.71 ± 0.03	20.55 ± 0.05
SEXTANS-A-s022	21.17 ± 0.02	20.40 ± 0.11
SEXTANS-A-s038	21.11 ± 0.02	20.44 ± 0.10
SEXTANS-A-s029	20.90 ± 0.05	20.39 ± 0.20
SEXTANS-A-s037	21.11 ± 0.05	20.52 ± 0.22
SEXTANS-A-SA2	21.07 ± 0.03	20.23 ± 0.21
SEXTANS-A-s021	20.38 ± 0.04	20.38 ± 0.20

Notes.
[a] $\log N(\mathrm{H\,I})$ of IC 1613/Sextans A toward a listed sight line.
[b] $\log N(\mathrm{H\,I})$ of Milky Way toward a listed sight line.

3. Gas-phase Column Density Measurements

In this section, we describe the novel line profile fitting method used to perform ISM abundance measurements from the METAL-Z data. The measurements were performed only for Fe II and S II lines (parameters of observed lines are summarized in Table 3); other metal lines were either too saturated or undetected (Section 2.2). In addition, we describe the measurements of the H I column density through line profile fitting of the Lyα line.

Alongside the profile fitting, we have implemented a curve of growth (CoG) method to measure the column density of S and Fe from METAL-Z data. Due to the resolution of COS and the limited S/N of the data, the CoG resulted in highly scattered measurements with large error bars. We present the results of these measurements in Appendix A to illustrate that the CoG method does not provide sufficiently accurate results from these spectra to pursue our analysis of the variations of depletions and D/G.

3.1. Measurements of the Atomic Hydrogen Column Density

The hydrogen column density N(H) is used to normalize metal abundances. The total N(H) includes contributions from hydrogen in atomic (H I) and molecular (H_2) forms. The fraction of the latter in the cold ISM varies with gas column density and metallicity (Tumlinson et al. 2002).

METAL-Z galaxies are sufficiently separated in velocity from the MW ($-233\,\mathrm{km\,s^{-1}}$ for IC 1613 and $324\,\mathrm{km\,s^{-1}}$ for

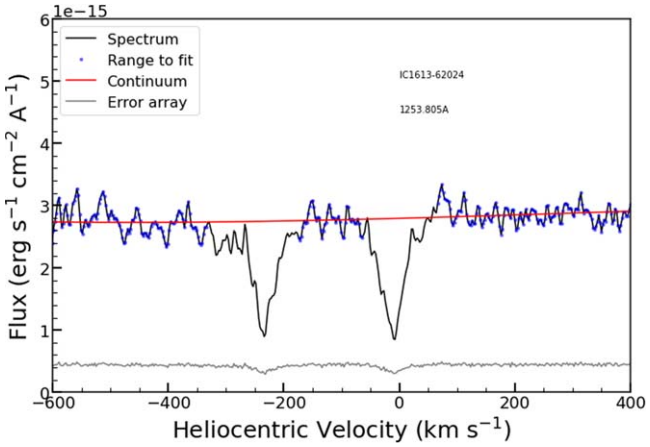

Figure 3. An example of continuum fitting procedure. The spectrum (black) is centered on the line of interest (here, S II λ1253 Å) in the Milky Way velocity frame while the S II from IC 1613 is visible around -200 km s^{-1}. Blue dots mark regions of the spectrum included in the fit; the red line shows the polynomial fit to the continuum. We selected the fitting windows to exclude Milky Way, ISM, and stellar lines.

Sextans A) to use the Lyα λ1216 Å absorption line for N(H I) measurements. We measured N(H I) by modeling the Lorentzian absorption profile of the Lyα line using two components, one for the MW and one for the galaxy of interest (Sextans A or IC 1613). We used a modified continuum reconstruction method outlined in Diplas & Savage (1994), Roman-Duval et al. (2019), which we summarize in this section (method illustrated in Figure 2).

First, we determined the heliocentric velocities of the MW and the galaxy toward a specific sight line by measuring the velocity offsets of the S II λ1250 Å absorption line from its rest-frame wavelength for both the MW and METAL-Z galaxies. These velocity offsets were adopted as central velocities for their respective Lyα absorption components. Second, we fitted a linear function to the continuum around the Lyα line, excluding ISM, photospheric, and stellar wind lines, such as the N V P Cyg profile around λ1240 Å, from the fits. We then normalized the spectra using this linear continuum. Third, we modeled the Lyα profile in the normalized spectra using two Lorentzian profiles, one for the MW and one for IC 1613/Sextans A using the velocities derived from S II in the first step. The profile fits were performed by minimizing the χ^2 between the observed absorption profile and a two-dimensional grid of two-component Lorentzian model profiles sampling the MW and galaxy H I column density (N(H I)$_{\rm MW}$ and N(H I)$_{\rm gal}$). The grid covers a range of column densities log N(H I) = 18.5–22.5 cm^{-2} for each of the components (MW and IC 1613/Sextans A). We excluded ISM metal absorption lines, stellar absorption lines, and the very bottom trough of the Lyα absorption profile, which has zero or negative counts, from the fits by manually selecting the spectral windows included in the χ^2 estimation. The fitting resulted in N(H I) measurements for both the MW and galaxy along each METAL-Z sight line. The measured log N(H I) values ranged from $\sim$20.5 to $\sim$21.2 cm^{-2} and are presented in Table 4.

To estimate the uncertainties of the N(H I) measurements, we translated the χ^2 to a two-dimensional likelihood $L \sim \exp(-\chi^2/2)$. Following Lampton et al. (1976) and given our two parameters (N(H I)$_{\rm MW}$ and N(H I)$_{\rm gal}$), we adopted $L_{1\sigma} = L_{\rm max} \times 0.32$, corresponding to $\chi^2 = \chi_{\rm min} + 2.3$, as the 1σ uncertainty.

We estimated the molecular gas fraction for our sight lines based on measured N(H I) and the dependence of the molecular gas fraction on hydrogen column density observed in the LMC and SMC in Welty et al. (2012). In the SMC, which has the closest metallicity to our sample, the molecular gas fraction rapidly decreases below log N(H) = 21.8 cm^{-2} (see Figure 17 in Welty et al. 2012). Below this threshold column density, the molecular fraction is only a few percent or less. Based on the H I measurements described above, the H_2 fraction toward our sight lines, which have even lower metallicity than the SMC, should be at most a few percent and can be neglected. At the same time, the contribution from ionized hydrogen (H II) at neutral column densities typical of our sample (N(H I) > 19.5 cm^{-2}) is $\ll$1% (Tchernyshyov et al. 2015). Therefore, we adopt the atomic hydrogen column density N(H I) as a measure of total gas density N(H).

3.2. Continuum Fitting around Metal Absorption Lines

We fitted third-order Legendre polynomials (following the fitting approach in Sembach & Savage 1992; Jenkins 1996) to the continuum around each measured line, within $\pm$ 1000–1500 km s^{-1} from the line center. Figure 3 shows an example of a continuum fit. We followed the error estimation method described in Sembach & Savage (1992) to calculate the continuum fit errors. In summary, this method considers errors in the flux measurements and the Legendre polynomial fitting and, following the standard χ^2 statistic, provides the error estimation on the continuum fit. The error on the continuum is added in quadrature with other sources of uncertainties (e.g., intensity error) in the measurements.

3.3. Column Density Measurements with Forward Optical Depth Modeling

We make two nonstandard choices in our method for measuring column densities. These choices are motivated by the relatively low S/N of part of the data set and by the large width of the COS line spread function (LSF), which have a full width at half-maximum (FWHM) of about 16 km s^{-1}, compared to the typical width of a metal line arising in the neutral ISM (FWHM of 3–10 km s^{-1}).

To deal with the low S/N, we use a Poisson likelihood function and work with photon counts instead of using a Gaussian likelihood function and working with fluxes. To avoid model selection issues in Voigt profile fitting, we create a mix of that technique with the apparent optical depth (AOD) method (Savage & Sembach 1991).

3.3.1. The Likelihood Function

The natural noise model for a photon-counting detector is the Poisson distribution. At high count rates, the normal distribution becomes an acceptable approximation to the Poisson distribution. For some of the Sextans A spectra in the data set, the typical number of photons at the continuum around the 1140 Å Fe II lines is 10, too low a number for an uncorrected normal approximation to be accurate.

Our solution to this issue is to use the Poisson distribution instead. Let $f[\lambda]$[6] be a model of spectrum flux, $T[\lambda]$ be the instrumental sensitivity function multiplied by the integration time, and $b[\lambda]$ be the expected number of background photon

[6] $X[\lambda]$ is the value of a quantity X at a pixel with central wavelength λ.

counts. The expected number of photon counts $\mu[\lambda]$ is equal to $f[\lambda] \times T[\lambda] + b[\lambda]$. The likelihood function for observed counts $c[\lambda]$ is a Poisson distribution with the rate parameter $\mu[\lambda]$.

3.3.2. Forward Optical Depth Modeling

The advantage of the AOD method is that it is nonparameteric; the advantage of Voigt profile fitting is that it accounts for the LSF through forward modeling. We propose the forward optical depth (FOD) method, in which the optical depth distribution is described using a dense set of basis functions (as in to AOD) instead of using a small number of flexible basis functions (as in Voigt profile fitting). The basis functions we use are Gaussians with fixed b parameters and centroids placed densely over velocity regions that are expected to contain absorption. The absorption model is specified by choosing the amplitude of each Gaussian.

To perform Bayesian inference using this setup, it is necessary to define a prior over the amplitudes. Allowing negative amplitudes would be unphysical. Constraining amplitudes to be strictly positive would mean that there would be some absorption at every velocity covered by a basis element. We use a solution inspired by the "spike and slab" family of priors (Ishwaran & Rao 2005), which combines a broad distribution away from zero (the slab) with a delta function at zero (the spike).

A scale parameter s, which we will see corresponds to the prior in the column density as a function of velocity $N(v)$, follows a uniform prior between $s_{\rm min}$ and $s_{\rm max}$. The pseudoamplitudes of the basis functions, $a[v]$, follow a Normal prior with mean zero and variance e^{2s}:

$$s \sim \text{Uniform}(s_{\rm min}, s_{\rm max}) \tag{2}$$

$$a[v] \sim \text{Normal}(0, e^{2s}). \tag{3}$$

Let G be the matrix or operator that multiplies the Gaussians that make up the basis by the pseudoamplitudes and sums them, and let $y[v] = Ga[v]$. The column density as a function of velocity $N[v]$ is $y[v]$ when $y[v]$ is positive and zero otherwise:

$$N[v] = \begin{cases} 0 & y[v] \leqslant 0 \\ y[v] & y[v] > 0. \end{cases} \tag{4}$$

The resulting prior over positive $N[v]$ is uniform in $\log N[v]$ between $s_{\rm min}$ and $s_{\rm max}$ with tails extending below $s_{\rm min}$ and above $s_{\rm max}$. There is also a spike at $N[v] = 0$, which contains half the total probability mass. The results are not sensitive to the exact values of $s_{\rm min}$ and $s_{\rm max}$ so long as $s_{\rm min}$ corresponds to a line depth too small to detect, and $s_{\rm max}$ corresponds to at least the largest plausible column density.

It is also necessary to choose the width of the Gaussians and their spacing. We use a b parameter of $2\,{\rm km\,s^{-1}}$. This is narrower than most Fe II and S II absorption components seen in high-resolution spectra of the neutral ISM (Welty et al. 1997). We find that using $b = 1$ or $1.5\,{\rm km\,s^{-1}}$ does not change the results of numerical experiments (but does require a longer computation time). The component centroids are separated by a factor of FWHM/3 (i.e., $1.57\,{\rm km\,s^{-1}}$ for $b = 2\,{\rm km\,s^{-1}}$), and the spectral synthesis is done on a wavelength grid with pixel separation smaller than FWHM/3.

3.3.3. Complete Model

The absorption model uses the FOD parameterization described above with Gaussian basis elements covering foreground and target galaxy velocity ranges. For IC 1613, the foreground range is from -75 to $+50\,{\rm km\,s^{-1}}$, and the target galaxy range is from -300 to $-200\,{\rm km\,s^{-1}}$. For Sextans A, the foreground range is from -75 to $+200\,{\rm km\,s^{-1}}$, and the target galaxy range is from $+220$ to $+420\,{\rm km\,s^{-1}}$. The foreground range for Sextans A is wider because of the presence of strong high-velocity cloud absorption in the spectrum.

To marginalize over continuum placement uncertainties, the model includes the coefficients of a degree two polynomial perturbation about the continuum derived in Section 3.2. The absorption and continuum models are multiplied to produce a complete flux model, and the complete flux model is used to compute the likelihood function as is described in Section 3.3.1.

We implement the model in the `numpyro` probabilistic programming language. The posterior probability density function over the model parameters is explored through Markov Chain Monte Carlo (MCMC) sampling using the `numpyro` implementation of the No U Turns Sampler (Hoffman & Gelman 2014). For each problem, we generate three independent MCMC chains running each for 200 (subsequently discarded) burn-in steps and 500 kept steps. We assess the convergence using the rank-normalized $\hat{R}$ statistic (Vehtari et al. 2021).

Figures 4 and 5 show examples of fits to absorption toward stars in Sextans A and IC1613. We summarize the estimated total column densities $\log_{10} N$ in the target galaxies by taking means and standard deviations of the posterior probability distributions over $\log_{10} N$. These values are reported in Table 5.

To test the reliability of the column density estimates, we create artificial spectra with known input column densities and use different methods to try to recover the inputs. These numerical experiments are described in Appendix B.

3.4. Gas-phase Abundances and Depletions of Fe and S

We calculated gas-phase abundances of Fe and S by taking the ratio of the measured column densities to the total hydrogen column densities derived in Section 3.1. We assume that an element's total (gas + dust) abundance is equal to that element's abundance in the photospheres of young stars recently formed in the ISM. By comparing measured abundances from the gas phase with the abundances in stellar photospheres, we can derive the fraction of metal locked in the dust (see Equation (1)).

The stellar abundances used in this work, alongside their sources in the literature, are summarized in Table 6. Both METAL-Z galaxies have measured stellar Fe abundances. We note that the stellar abundance of Fe in IC 1613 reported in the literature varies between $[{\rm Fe/H}] = -0.3$ and 0.8 (see Garcia et al. 2014, for full discussion). Here, we adopted the value of $[{\rm Fe/H}] = -0.69$ (Bouret et al. 2015), consistently found in massive stars.

IC 1613 and Sextans A lack direct measurements of S stellar abundances. Therefore, we used other α elements as the reference, assuming their abundance relative to solar is comparable to S. We used O for IC 1613 (Bresolin et al. 2007), and Mg in Sextans A (Kaufer et al. 2004, as it does not

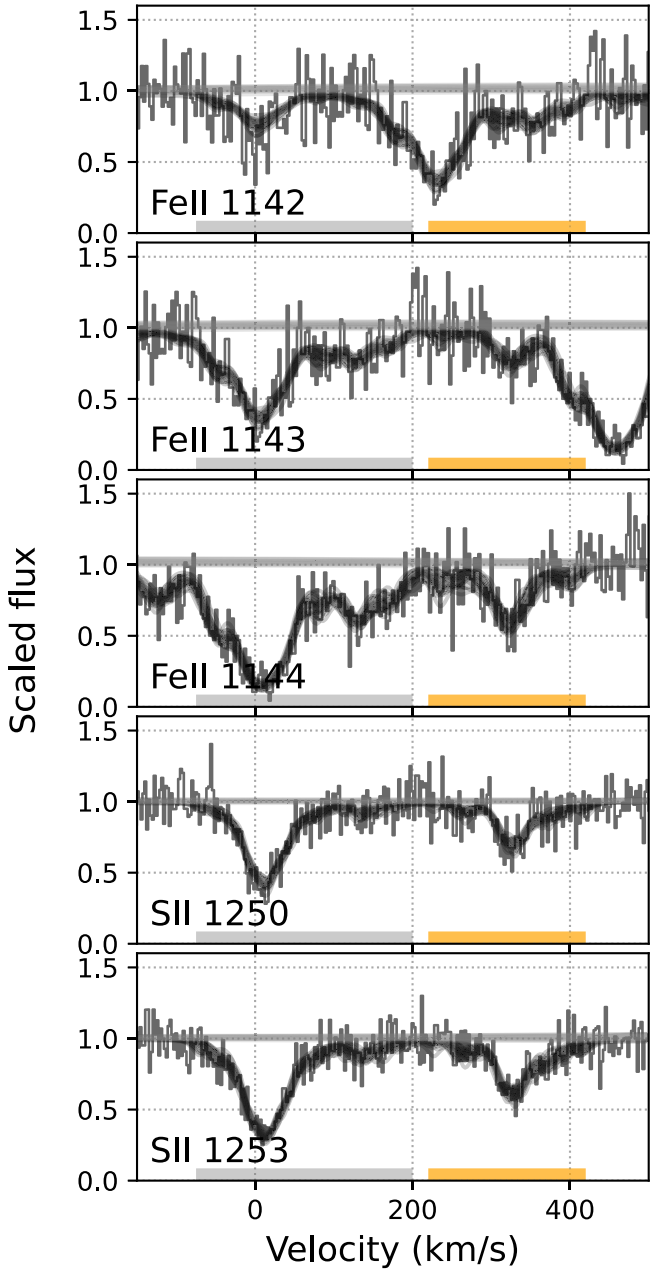

Figure 4. Forward optical depth method fits to Fe II and S II absorption toward the star SEXTANS-A-s022. The velocity ranges of foreground Milky Way and Sextans A-associated gas are indicated by gray and orange horizontal bars. The observed spectrum is shown using a stepped gray line, continuum uncertainty is shown using smooth gray lines, and the absorption model is shown using black lines.

have a measured O stellar abundance either), and assumed [S/H] ≃[O/H] ≃[Mg/H].

4. The Dependence of Depletions on Gas Density and Metallicity

In this section, we examine the dependence of metal depletion on gas density and metallicity, since these two parameters are expected to drive the dust growth timescale in the ISM (Asano et al. 2013; Zhukovska et al. 2016). We present the relation between the depletion of Fe and S in Section 4.1 and their dependence on the hydrogen column density and metallicity in Section 4.2.

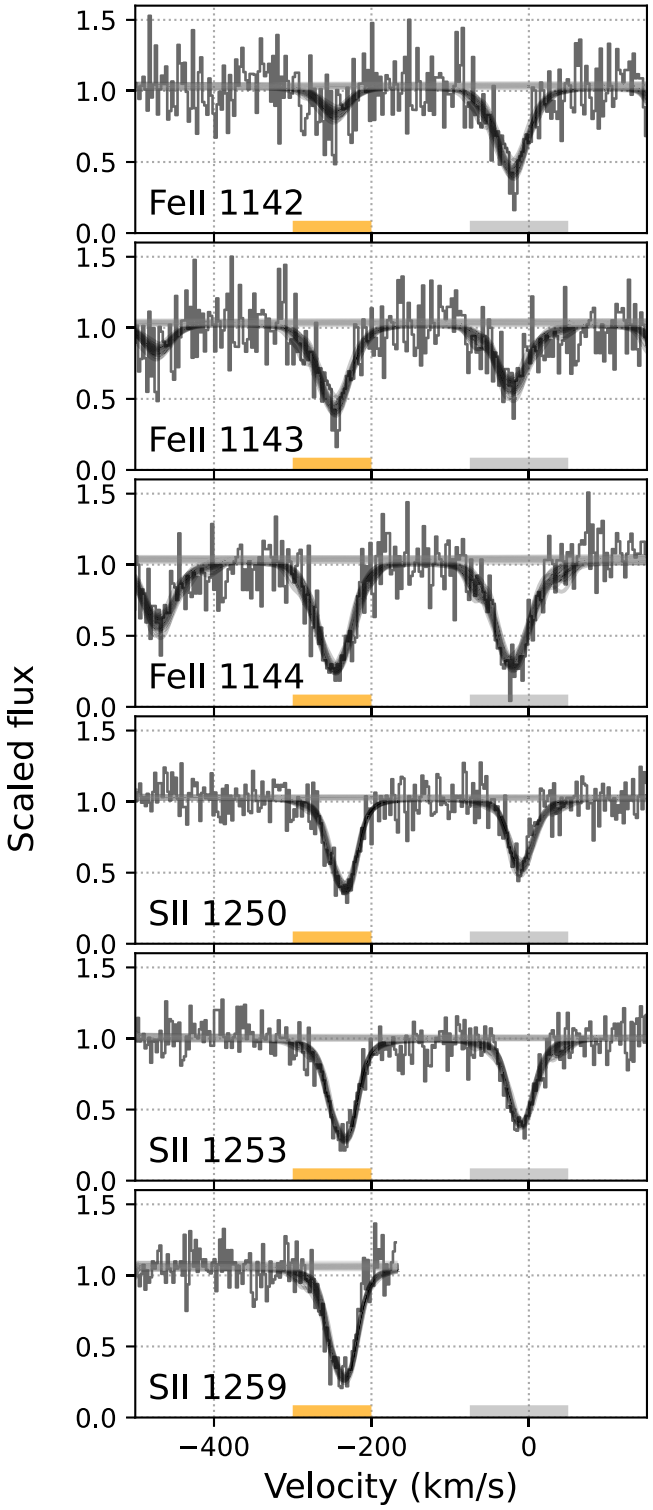

Figure 5. Forward optical depth model fits to Fe II and S II absorption toward the star IC1613-B2. The velocity ranges of foreground and IC1613-associated gas are indicated by gray and orange horizontal bars. The observed spectrum is shown using a stepped gray line, continuum uncertainty is shown using smooth gray lines, and the absorption model is shown using black lines.

4.1. Relation between Depletions of Different Elements

Jenkins & Wallerstein (2017), Roman-Duval et al. (2021), and Roman-Duval et al. (2022a) have shown a strong correlation between the depletion of various elements and that of Fe in the SMC and LMC, respectively, and that this

Table 5
Column Density, Fe, and S Depletions for METAL-Z Sight Lines

Target	log N(H) (cm^{-2})	log N(S II) (cm^{-2})	log N(Fe II) (cm^{-2})	δ(S)	δ(Fe)
IC1613-61331	20.84 ± 0.03	15.35 ± 0.05	14.59 ± 0.06	0.04 ± 0.06	-1.12 ± 0.07
IC1613-62024	21.05 ± 0.03	15.54 ± 0.07	14.84 ± 0.07	0.02 ± 0.08	-1.08 ± 0.08
IC1613-64066	20.88 ± 0.04	15.43 ± 0.06	14.80 ± 0.07	0.08 ± 0.07	-0.95 ± 0.08
IC1613-67559	20.47 ± 0.14	15.16 ± 0.07	14.61 ± 0.06	0.22 ± 0.15	-0.73 ± 0.15
IC1613-67684	20.44 ± 0.04	14.97 ± 0.07	14.54 ± 0.07	0.06 ± 0.08	-0.77 ± 0.08
IC1613-A13	20.26 ± 0.03	15.11 ± 0.08	14.69 ± 0.09	0.38 ± 0.09	-0.44 ± 0.09
IC1613-B11	20.37 ± 0.05	15.19 ± 0.07	14.41 ± 0.08	0.35 ± 0.09	-0.83 ± 0.09
IC1613-B2	21.17 ± 0.03	15.65 ± 0.07	14.99 ± 0.06	0.01 ± 0.08	-1.05 ± 0.07
IC1613-B3	20.64 ± 0.06	15.28 ± 0.08	14.49 ± 0.08	0.17 ± 0.10	-1.02 ± 0.10
IC1613-B7	20.73 ± 0.03	15.24 ± 0.05	14.71 ± 0.04	0.04 ± 0.06	-0.89 ± 0.05
SEXTANS-A-s050	20.46 ± 0.04	15.17 ± 0.05	14.74 ± 0.07	0.54 ± 0.06	-0.27 ± 0.08
SEXTANS-A-s014	20.71 ± 0.03	15.06 ± 0.07	14.70 ± 0.09	0.18 ± 0.08	-0.56 ± 0.09
SEXTANS-A-s022	21.17 ± 0.02	15.35 ± 0.07	14.73 ± 0.09	0.01 ± 0.08	-0.99 ± 0.09
SEXTANS-A-s038	21.11 ± 0.02	15.27 ± 0.05	14.86 ± 0.07	-0.01 ± 0.06	-0.80 ± 0.07
SEXTANS-A-s029	20.90 ± 0.07	15.13 ± 0.08	14.69 ± 0.12	0.06 ± 0.11	-0.76 ± 0.14
SEXTANS-A-s037	21.11 ± 0.07	15.29 ± 0.09	15.08 ± 0.12	0.01 ± 0.11	-0.58 ± 0.14
SEXTANS-A-SA2	21.07 ± 0.04	15.39 ± 0.07	14.98 ± 0.10	0.15 ± 0.08	-0.64 ± 0.11
SEXTANS-A-s021	20.38 ± 0.04	15.29 ± 0.10	14.72 ± 0.11	0.74 ± 0.11	-0.21 ± 0.11

Table 6
Stellar Abundances of METAL-Z Galaxies

Galaxy	[Fe/H]	[α/H]
IC 1613	-0.67 ± 0.09 (a)	-0.79 ± 0.08 (b)
Sextans A	-0.99 ± 0.04 (c)	$-1.09^{+0.02}_{-0.19}$ (c)

Note. Due to lack of S abundance measurements, we adopted $\alpha = O$ for IC 1613, and $\alpha = Mg$ for Sextans A.
References. (a) Tautvaišienė et al. (2007), (b) Bresolin et al. (2007), (c) Kaufer et al. (2004).

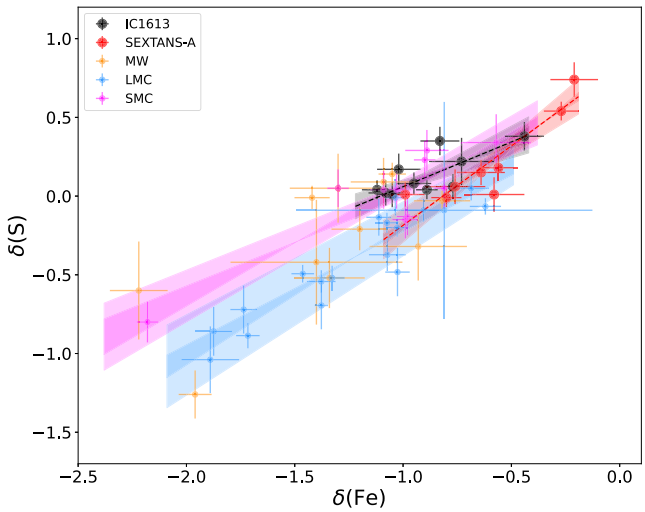

Figure 6. Elemental depletions of sulfur vs. iron. METAL-Z measurements of depletion of these two elements are shown in black (IC 1613) and red (Sextans A). Depletions of S and Fe derived in the MW (Jenkins 2009), LMC (Roman-Duval et al. 2021), and SMC (Jenkins & Wallerstein 2017) are also shown in orange, blue, and magenta, respectively. For each set of measurements, a linear fit and associated uncertainties are shown in transparency. The relation between δ(S) and δ(Fe) in IC 1613 and Sextans A follows the trends observed in the LMC and SMC, with IC 1613 being closer to the SMC and Sextans A to the LMC. We note that $\delta(S) > 0$ indicates no sulfur depletion at metallicities below 20% solar. The all-positive depletions of sulfur can result from uncertain stellar abundances in IC 1613 and Sextans A and/or a contribution from ionized gas to S II.

correlation weakly depends on metallicity, at least in the MW, LMC, and SMC. There are some exceptions: Roman-Duval et al. (2022a) showed that Ti and Mg deplete less relative to Fe in the Magellanic Clouds compared to the MW, while Jenkins & Wallerstein (2017) found that Mn depletes more rapidly relative to Fe in the SMC than in the MW.

Fe column densities are easier to measure than those from other elements, thanks to their multiple transitions with varying oscillator strengths throughout the UV range. An invariance of the relation between depletions of different elements with metallicity would therefore prove very useful in estimating the depletions for dust-building elements from Fe depletions alone in low-metallicity, more distant systems where other UV lines may not be detected.

We test the invariance of the relation between Fe and S depletions with metallicity down to $Z = 0.1 Z_{\odot}$ using the METAL-Z observations. In Figure 6, we plot the Fe and S depletion measurements for IC 1613 and Sextans A, as well as the relation between δ(Fe) and δ(S) derived in the MW, LMC, and SMC. The measurements obtained in IC 1613 and Sextans A are consistent with the trends established in the MW, LMC, and SMC, with all trends within 2σ of each other (as shown by the overlap between the transparent bands representing the linear relations and their 1σ uncertainties in Figure 6). The linear relation between δ(Fe) and δ(S) in IC 1613 is slightly closer to that observed in the SMC, while that same relation observed in Sextans A is in marginally better agreement with measurements in the LMC. This result suggests that there is no significant evolution of this trend with metallicity, within the uncertainties. This is a good indication that the relation between the depletions of different elements at the first order may not significantly vary with metallicity. This will allow us later in the paper to assume the MW relation between the depletion of Fe and other elements to estimate D/G in IC 1613 and Sextans A based on the measured Fe depletions in those galaxies (see Section 5). We note, however, that the METAL-Z program only probes S and Fe, and that neither METAL-Z nor

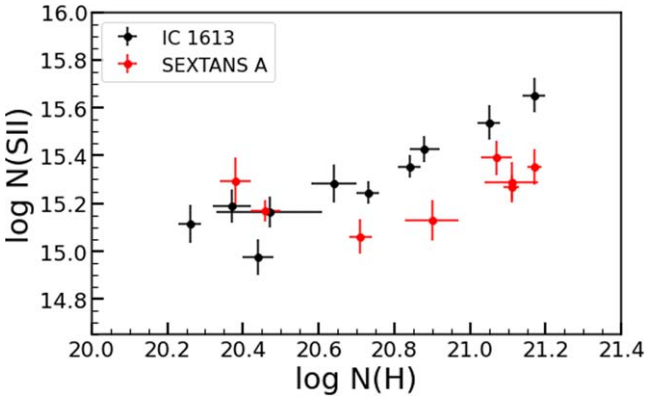

Figure 7. Column density measurements of S II and H in IC 1613 (black) and Sextans A (red). The expected linear relation between the column density of sulfur and hydrogen flattens at low gas densities of log N(H) $<$20.6 cm^{-2}. Unexpectedly high N(S II) happening mostly at lower N(H) can be explained by an ionized layer of gas that is subdominant at high gas densities but apparent at lower values of N(H).

previous studies in the LMC and SMC included the major source of metal and dust mass: carbon and oxygen.

The depletions toward sight lines in IC 1613 and Sextans A vary between −1.1 to −0.2 for δ(Fe) and 0 to 1 for δ(S). The $\delta(S) > 0$ measurements would indicate no sulfur depletion, but there remains the possibility of slightly depleted slight lines if the stellar abundances of sulfur are underestimated. Indeed, stellar abundances of sulfur are not directly measured. Instead, we assumed [S/H] = [Mg/H] in Sextans A, and [S/H] = [O/H] in IC 1613 (see Section 3.4 and Table 6).

Another possible explanation for the positive depletions of S in IC 1613 and Sextans A is the contribution of ionized gas to S II. Since S II has a significantly higher ionization potential than hydrogen (23 eV), S II in ionized gas surrounding the target O or early B star may contribute significantly to the S II column density. In Figure 7, we show the relation between column densities of S II and H. At log N(H) $<$ 20.6 cm^{-2}, the otherwise linear relation flattens, resulting in higher measurements of log N (S II) than expected, signifying a contamination from ionized gas. Since abundances are only normalized to H, this would result in overestimated gas-phase abundances. For sight lines that are only very mildly depleted in S, as in the case of the low metallicities observed here, the contamination of N(S II) by ionized gas would, therefore, result in positive depletions δ (S) > 0 (Jenkins 2009; Jenkins & Wallerstein 2017).

Positive S depletions are seen up to gas column densities log N(H I) ∼21 cm^{-2} in IC 1613 and Sextans A. For this reason, measurements of sulfur depletions cannot be used to draw robust conclusions. Because of the positive S depletions $\delta(S) > 0$, we do not attempt to fit the δ(Fe)–δ(S) relation for IC 1613 and Sextans A.

4.2. The Variations of Fe and S Depletion with Hydrogen Column Density and Metallicity

The timescale for the accretion of gas-phase metals onto dust grains is inversely proportional to the metallicity and the gas density (Asano et al. 2013; Zhukovska et al. 2016). Therefore, we expect to find a metal depletion and dust abundance dependence on these parameters. Depletion studies in the MW, LMC, and SMC have shown that the fraction of metals in the gas (depletion) decreases with increasing N(H) (Wakker & Mathis 2000; Jenkins 2009; Tchernyshyov et al. 2015; Roman-Duval et al. 2021, 2022a) in systems down to a metallicity of 20% solar. This indicates that the fraction of metals locked in dust, and subsequently the abundance of dust, increases with increasing gas density owing to the accretion of gas-phase metals onto dust grains as the ISM becomes denser. We would expect similar trends in lower-metallicity galaxies such as those observed as part of METAL-Z.

For a face-on galaxy, variations in hydrogen column density are caused by density fluctuations in the medium and changes in the scale length perpendicular to the galaxy disk. Roman-Duval et al. (2022a) argued that the magnitude of path length variations in the LMC is negligible. Therefore, the variations in N(H) between the lines of sight probe the variations in the mean gas density along those sight lines. We assume the same is true for IC 1613 and Sextans A, with inclinations of 38° and 33°, respectively (Hunter et al. 2012), and that N(H) represents the average behavior of the gas density structure in the ISM of these objects.

For the LMC, SMC, and MW, Roman-Duval et al. (2021, 2022a) introduced a linear relation between metal depletion and log N(H):

$$\delta(\mathrm{X}) = B_{\mathrm{H}}(\mathrm{X}) + A_{\mathrm{H}}(\mathrm{X})(\log N(\mathrm{H}) - \log N_{\mathrm{H}_0}(\mathrm{X})) \quad (5)$$

where A_{H} is the slope of the linear relation, B_{H} is the zero-point, and $\log N_{\mathrm{H}_0}(\mathrm{X})$ is a weighted mean hydrogen column density computed for each sample galaxy and element X. $\log N_{\mathrm{H}_0}(\mathrm{X})$ is introduced to remove the covariance between the intercept and the slope of the linear function and is defined as follows:

$$\log N_{\mathrm{H}_0}(\mathrm{X}) = \frac{\sum_{\mathrm{l.o.s}} \frac{\log N(\mathrm{H})}{\sigma(\delta(\mathrm{X}))^2}}{\sum_{\mathrm{l.o.s}} \frac{1}{\sigma(\delta(\mathrm{X}))^2}} \quad (6)$$

where the sum is performed over all lines of sight in a given galaxy, and $\sigma(\delta(\mathrm{X}))$ is the uncertainty on the depletion measurement of X along each sight line.

The zero-points of the relation between hydrogen column density and depletions, i.e., B_{H} as well as the intercept of the linear relation given by $B_{\mathrm{H}} - A_{\mathrm{H}} \log N_{\mathrm{H}_0}(\mathrm{X})$, are observed to increase with decreasing metallicity in the MW, LMC, and SMC (Roman-Duval et al. 2022a), indicating that, for a given gas density, metals become less depleted from the gas phase as the total metallicity decreases. As a result, Roman-Duval et al. (2022a) showed that the gas-phase metallicity of the SMC is similar to the gas-phase metallicity of the MW, because, while the metallicity of the SMC is 5 times lower than that of the MW, the fraction of metals in the gas is also 5 times higher than in the MW.

To test how metals deplete in the lower-metallicity galaxies IC 1613 and Sextans A, we fitted a similar linear function to the relation between Fe depletions and log N(H) measured in those galaxies. We used a Bayesian linear regression method to find the best-fit parameters A_{H} and B_{H} and estimate their uncertainties. To create the model, we constructed a grid of coefficient values for the slope, A_{H} (ranging from −1 to 1), and the zero-point B_{H} (ranging from −2 to 2). For A_{H} and B_{H} parameters, we used flat priors limited to the grid range.

We adopted the parameter pair with the highest probability (the smallest χ^2 as the best-fitting model). We used the Lampton et al. (1976) method to establish the errors and adapted a $\chi^2 = \chi_{\mathrm{min}} + 2.3$ as the 1σ uncertainty. The derived fit parameters for METAL-Z galaxies are listed in Table 7. In Figure 8, we show the fitted relation between log N(H) and

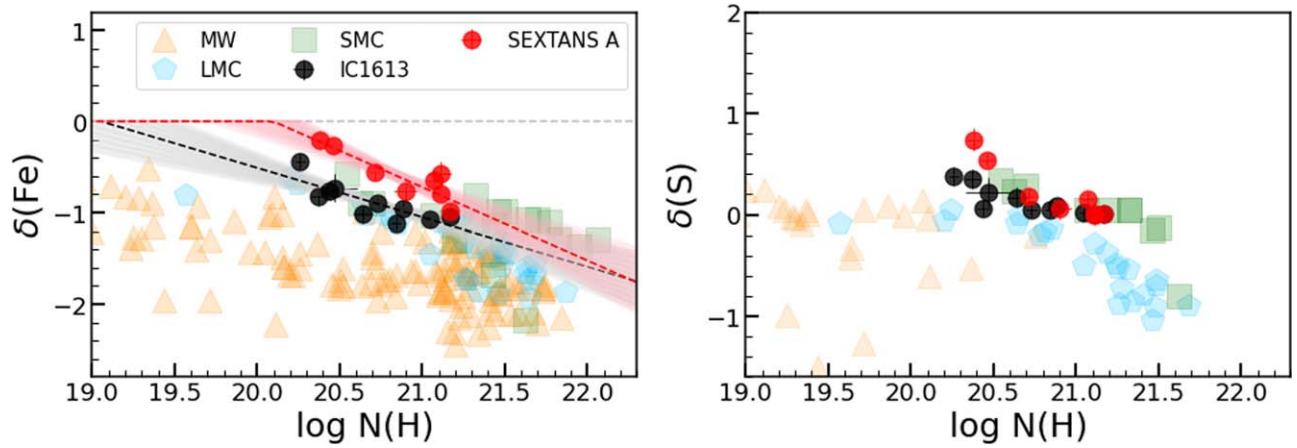

Figure 8. Relation between depletion of Fe (left), S (right), and hydrogen column density N(H). Galaxies in the METAL-Z sample are marked in red (Sextans A) and black (IC 1613). We compare our measurements with the literature: Milky Way (orange triangles, Jenkins 2009), LMC (blue pentagons, Roman-Duval et al. 2021), and SMC (green squares, Jenkins & Wallerstein 2017). In IC 1613 and Sextans A, iron depletion decreases with increasing column density, similar to trends in the MW, LMC, and SMC. We fit the linear relation between Fe depletions and log N(H) (dotted line) and show the uncertainties as shaded areas. Fe depletions also show a dependence on total metallicity: Sextans A, the lowest-metallicity galaxy in the sample, shows less depletion than higher-metallicity galaxies in the same N(H) range. The positive depletions of sulfur are consistent with no depletion and show no variation with gas column density.

depletion of Fe and compare them to the MW, LMC, and SMC measurements. Wherever the relation predicts $\delta(\mathrm{X}) > 0$, we plot $\delta(\mathrm{X}) = 0$ instead. As $\delta(S) > 0$ for both galaxies, we do not establish the relation with gas density for sulfur; we plot the depletion measurements in Figure 8.

From previous results in the MW, LMC, and SMC (Roman-Duval et al. 2022a), we expected to see two effects: (1) a decrease in iron depletion with increasing hydrogen column density (i.e., an increase in the fraction of metals locked in dust with increasing gas density) and (2) an increase in depletion value with decreasing galaxy metallicity (i.e., a decrease in the fraction of metals locked in dust with decreasing metallicity). The negative slopes of the relation between δ(Fe) and log N(H) show that, in the low-metallicity environments of IC 1613 and Sextans A, iron is indeed more depleted in the higher density ISM. The slopes A_{H}(Fe) in IC 1613 and Sextans A are -0.54 ± 0.19 and -0.80 ± 0.23, respectively, which is in line with the slopes reported by Roman-Duval et al. (2022a) in the MW (-0.41 ± 0.03), LMC (-0.71 ± 0.03), and SMC (-0.59 ± 0.04).

Simultaneously, the zero-point B_{H} of the relation between log N(H) and δ(Fe) increases with decreasing metallicity, with $B_{\mathrm{H}}(\mathrm{Fe}) = -0.91 \pm 0.04$ in IC 1613, and $B_{\mathrm{H}}(\mathrm{Fe}) = -0.61 \pm 0.06$ in Sextans A, compared to $B_{\mathrm{H}}(\mathrm{Fe}) = -1.62 \pm 0.02$ in the MW, -1.39 ± 0.01 in the LMC, and -1.18 ± 0.01 in the SMC (Roman-Duval et al. 2022a). Admittedly, B_{H}(Fe) corresponds to the depletion level at $\log N_{\mathrm{H}_0}$(Fe), which is the weighted mean hydrogen column density of each sample and varies from galaxy to galaxy. Therefore, the evolution of the B_{H}(Fe) parameter with metallicity is not an exact representation of the changes in the depletion zero-levels with metallicity. Therefore, we also report in Table 7 the Fe depletions at the lower and higher ends of the log N(H) range probed by the sample, log N(H) = 20.3 cm^{-3}, and log N(H) = 21 cm^{-2}. At log N(H) = 21 cm^{-2}, the Fe depletion level in the MW is -1.58 (Roman-Duval et al. 2022a), and thus, the Fe depletion value increases by 0.53 dex (factor of 3.4) from the MW to IC 1613 and by 0.86 dex (factor of 7.2) from the MW to Sextans A. This indicates that the zero-point level of depletions continues to increase (i.e., the fraction of metals locked in dust continues to decrease) as the metallicity decreases below that of the SMC (20% solar).

Table 7
Fitted Parameters A_{H}, B_{H}, and $\log N_{\mathrm{H}_0}$ of the Relation between Fe Depletion δ (Fe) and Hydrogen Column Density log N(H) for IC 1613 and Sextans A

	IC 1613	Sextans A
A_{H}(Fe)	-0.54 ± 0.19	-0.80 ± 0.23
B_{H}(Fe)	-0.91 ± 0.04	-0.61 ± 0.06
$\log N_{\mathrm{H}_0}$(Fe)	20.74	20.86
δ(Fe) at log $N = 20.3$ cm^{-2}	-0.67 ± 0.09	-0.16 ± 0.14
δ(Fe) at log $N = 21$ cm^{-2}	-1.05 ± 0.06	-0.72 ± 0.07

4.3. Evolution of the Iron Fraction in Dust with Metallicity

Having measured the depletions of Fe in IC 1613 and Sextans A, we compute the fraction of iron in dust and the "iron dust-to-gas mass ratio," D_{Fe}/G, given below:

$$D_{\mathrm{Fe}}/G = \frac{1}{1.36}(1 - 10^{\delta(\mathrm{Fe})})\left(\frac{N(\mathrm{Fe})}{N(\mathrm{H})}\right)_{\mathrm{tot}} W(\mathrm{Fe}), \qquad (7)$$

where W(Fe) is the atomic weight of iron. The $1 - 10^{\delta(\mathrm{Fe})}$ alone gives the fraction of Fe atoms locked in the dust form. D_{Fe}/G corresponds to the abundance of iron dust relative to gas.

In the top panel of Figure 9, we show the fraction of Fe locked in the dust at different gas densities. Alongside IC 1613 and Sextans A, we plot the fraction of Fe in dust for the MW, LMC, and SMC taken from Jenkins (2009), Roman-Duval et al. (2021), and Jenkins & Wallerstein (2017). The MW, LMC, and SMC show comparable fractions of Fe in dust ($\sim$1) for log N(H) $>$ 21.5 cm^{-2}. At lower column densities, the fraction of Fe in dust drops faster for lower-metallicity systems. This is expected, as the dust accretion timescale is inversely proportional to density and metallicity. IC 1613, with an iron content that is similar to the SMC, aligns with the Magellanic Clouds with 70%–80% of iron in dust at log N(H) = 20.5 cm^{-2}. In the lowest-metallicity system, Sextans A, the

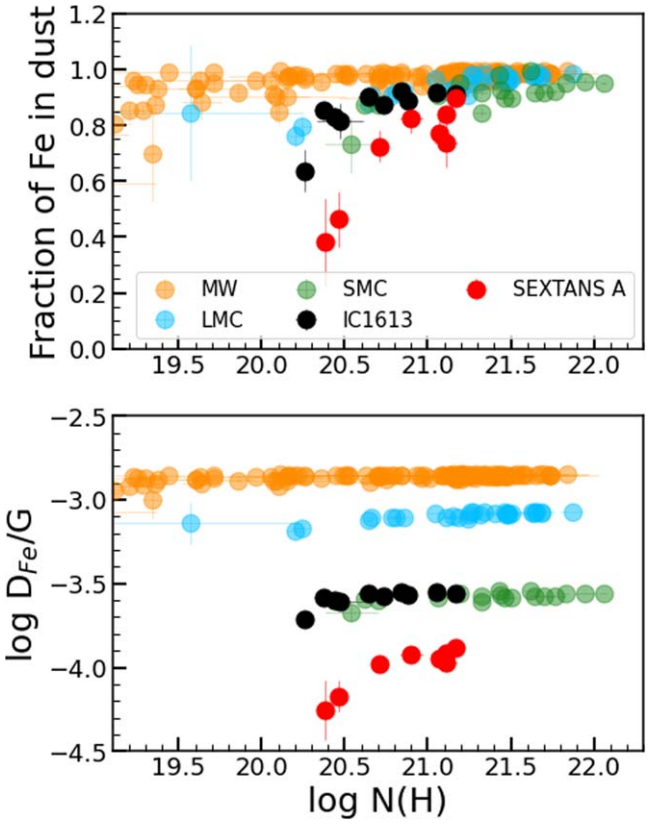

Figure 9. Fraction of Fe in dust vs. N(H) column density (top), and Fe dust-to-gas ratio (bottom). METAL-Z galaxies are marked in black (IC 1613) and red (Sextans A). Literature data from Roman-Duval et al. (2022a) is shown in orange for the Milky Way, cyan for the LMC, and green for the SMC.

fraction of Fe in the dust is about 0.1–0.4 dex lower than in IC 1613 and the Magellanic Clouds.

The bottom panel of Figure 9 shows $D_{\rm Fe}/G$ for the MW, LMC, SMC, IC 1613, and Sextans A, as a function of log N(H). While $D_{\rm Fe}/G$ in IC 1613 follows the trend observed in the SMC very closely, Sextans A has a $D_{\rm Fe}/G$ that is 0.5–70.5 lower than the SMC and IC 1613. Since $D_{\rm Fe}/G$ depends on the iron abundance and the fraction of iron in dust, some of these variations are purely due to the varying metal content of these galaxies (metallicity). For example, for Sextans A, the lower metallicity contributes a factor of 10 in the lower $D_{\rm Fe}/G$ compared to the MW. However, the $D_{\rm Fe}/G$ in Sextans A is 20 times lower than the MW because the fraction of Fe in dust also decreases with metallicity, as shown in Figure 9.

5. Estimation of *D/G* and *D/M* from Iron Depletion

In Section 4.1, we showed that the relation between the depletions of iron and sulfur in IC 1613 and Sextans A is consistent with that of the MW, LMC, and SMC (Section 4.1). The MW and Magellanic Clouds contain the depletions of many measured elements (Si, Mg, Ni, Cr, Zn, S, Ti) that correlate tightly with the depletion of Fe (Roman-Duval et al. 2022a). It is therefore not unreasonable to assume that the relation between the depletion of Fe and other elements in IC 1613 and Sextans A also closely follows the MW, LMC, and SMC relation. Under this assumption, Fe can be used as a tracer of the collective depletion level of various elements, from which D/G and D/M can be estimated.

In previous sections, we have also shown that (1) the depletion of Fe (i.e., the fraction of Fe in the gas phase) in IC 1613 and Sextans A decreases with increasing gas density with a slope consistent with that of the MW, LMC, and SMC; and (2) the zero-point of Fe depletions increases with decreasing metallicity from the MW to the LMC, SMC, IC 1613, and Sextans A. Since different elements deplete from the gas collectively, as shown by the tight correlations between the depletions of different elements observed in the MW, LMC, SMC (Roman-Duval et al. 2022a), and between Fe and S in IC 1613 and Sextans A (see Section 4.1), it is safe to infer that the variations in Fe depletions observed in IC 1613 and Sextans A indicate that the dust-to-metal ratio and therefore also the dust-to-gas ratio increases with increasing gas density, at a rate that is similar between galaxies spanning 10%–100% solar metallicity (the slopes of Fe depletions versus log N(H) are similar in all five galaxies). The variations of the Fe depletion zero-point imply that the dust-to-metal ratio decreases with decreasing metallicity. This, in turn, implies that the dust-to-gas ratio, given by $D/G = D/M \times {\rm Z}$, should decrease faster than metallicity.

The measurements of S and Fe depletions presented in this paper are not sufficient for the derivation of the dust-to-gas ratio in IC 1613 and Sextans A. But by using Fe as a proxy for the overall depletion level of other elements and by assuming that the MW relation between δ(Fe) and δ(X) is invariant with metallicity, one can estimate D/G and D/M from the iron depletions measured in IC 1613 and Sextans A, and investigate how D/G and D/M vary with gas density and metallicity down to $\sim$10% solar metallicity.

We note that C and O comprise most of the metal and dust mass. However, C and O depletions have only been measured in the MW, and even in the MW, the trend of C depletions with F_* (gas density) is quite uncertain due to the sparsity and large errors of the measurements (Jenkins 2009). Therefore, the invariance of the relation between C or O depletions and Fe depletions with metallicity has not been tested, not even in the LMC and SMC (Roman-Duval et al. 2022a). While assuming the invariance of the δ(Fe)–δ(C or O) relation with metallicity allows us to estimate D/G and D/M and explore their variations with metallicity down to a yet unexplored metallicity regime, it does introduce a significant systematic uncertainty on the derived D/G and D/M values. Further constraining the relations between depletions in low-metallicity environments requires the sensitivity of next-generation UV telescopes, such as the Habitable Worlds Observatory.

5.1. Estimation of the Dust-to-gas and Dust-to-metal Ratios

From this point of our analysis, we make the fundamental assumption that the relation between the depletion of Fe and other elements does not vary with metallicity in order to infer D/G and D/M in IC 1613 and Sextans A, using Equation (8) of Roman-Duval et al. (2022a):

$$D/G = \frac{1}{1.36}\sum_{\rm X}(1 - 10^{\delta({\rm X})})\left(\frac{N({\rm X})}{N_{\rm H}}\right)_{\rm tot} W({\rm X}) \qquad (8)$$

where $N({\rm X})/N({\rm H_{tot}})$ is the total abundance of an element X in the galaxy, and W(X) is the atomic weight of element X. We include different dust-building elements in the computation of D/G: C, O, Mg, Si, S, Ti, Cr, Ni, Cu, Zn, and Fe. The dust-to-metal ratio D/M gives the fraction of the mass of metals locked

Table 8
Abundances of Elements Included in D/G Calculations: Solar, and Scaled for IC 1613 and Sextans A

Element	W_X	12 + log(X/H)tot		
		MW (a)	IC 1613[a]	SEXTANS A[a]
		α elements[b]		
C	12.01	8.46	7.67	7.37
O	16.00	8.76	7.97	7.67
Mg	24.30	7.62	6.83	6.53
Si	28.10	7.61	6.82	6.52
S	32.06	7.26	6.47	6.17
		Fe peak elements[c]		
Ti	47.87	5.00	4.33	4.01
Cr	52.00	5.72	5.05	4.73
Fe	55.85	7.54	6.87	6.55
Ni	58.70	6.29	5.62	5.30
Cu	63.55	4.34	3.67	3.35
Zn	65.40	4.70	4.03	3.71

Notes.
[a] See Table 6 for references to stellar abundances.
[b] Alpha elements' abundances were scaled from O abundance in IC 1613 and Mg in Sextans A.
[c] Iron peak abundances were scaled from Fe abundance in both IC 1613 and Sextans A.
Reference. (a) Morton (2003).

in dust. It can be derived from $D/G = D/M \times Z$, or directly from Equation (9) of Roman-Duval et al. (2022a):

$$D/M = \frac{\sum_X (1 - 10^{\delta(X)}) \left(\frac{N(X)}{N_H}\right)_{tot} W(X)}{\sum_X \left(\frac{N(X)}{N_H}\right)_{tot} W(X)}. \quad (9)$$

We use the photospheric abundances of Fe and S in B supergiants listed in Table 6, and assume [X/H] = [Fe/H] for iron-peak elements (Fe, Zn, Ni, Cr), and [X/H] = [Mg/H] (Sextans A) or [O/H] (IC 1613) for α elements (C, O, Si, Mg, Ti). Such derived abundances, together with reference solar abundances, are listed in Table 8.

To compute the depletions of elements other than Fe, we assume that the relation between δ(Fe) and δ(X) in IC 1613 and Sextans A is the same as for the MW (Jenkins 2009), where depletions for all those elements are measured. This assumption is based on the facts that (1) the relation between Fe and S depletion for METAL-Z galaxies is consistent with that derived for the MW and Magellanic Clouds (see Section 4.1), and (2) that Roman-Duval et al. (2022a) showed that the relation between the depletion of different elements and that of Fe does not vary significantly with metallicity (except for Mg, Ti, and Mn, see Section 4.1). Therefore, as a zeroth-order approximation, we assume the same is true for METAL-Z galaxies. Thus, we compute F_* from the fitted relation of δ(Fe) versus log N(H) (described in Section 4.2) in IC 1613 and Sextans A using the A_{Fe}, B_{Fe}, and z_{Fe} given in Jenkins (2009). The F_* parameter, introduced by Jenkins (2009) to describe the collective behavior of the depletion in MW, provides a good reference frame for comparing depletion of different elements. The F_* relates to depletion through a linear relation.

$$\delta(X) = A_x \times (F_* - z_x) + B_x \quad (10)$$

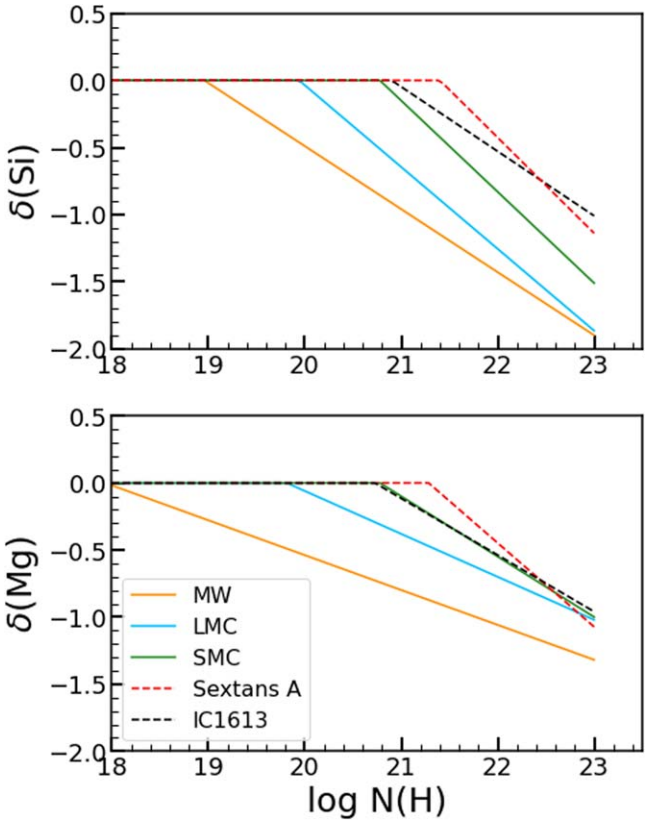

Figure 10. Depletion of Si (top) and Mg (bottom) as a function of log N(H) in the MW (orange), LMC (blue), SMC (green), IC 1613 (black), and Sextans A (red). In the MW and Magellanic Clouds, the relations were taken directly from the fits given in Roman-Duval et al. (2022a). We derived those relations in IC 1613 and Sextans A based on (1) the measured Fe depletions and (2) the MW relation between Fe depletion and depletion of other elements (since Si and Mg were not measured as part of METAL-Z observations). Such relations were derived for all main constituents of dust in order to estimate the D/G-ratio for METAL-Z galaxies.

where the A_x (slope), B_x (zero-point), and z_x (zero-point reference displacement) coefficients are given in Jenkins (2009). Then, we calculated δ(X) from F_* for other elements (Si, Mg, S, C, O, Zn, Ti, Cr, Cu, and Ni) using the relevant A_x, B_x, and z_x coefficients derived in Jenkins (2009) for the MW.

We obtain relations between δ(X) and log N(H) for all elements accounted for in the D/G. We do not allow positive depletion values; the extrapolated relations between depletion and gas density are set to zero for $\delta(X) > 0$.

We use a Monte Carlo method to propagate uncertainties from the fitted relation between log N(H) and δ(Fe) to the extrapolated relations between δ(X) and log N(H). We sampled from the Gaussian distributions of the coefficients from the relations between δ(Fe)–F_* and δ(X)–F_*. Assuming that the intercept and slope of the relationship are not covariant, we generated all possible relations that fit the data points and selected the one at 1σ deviation from the linear relationship used as the final uncertainty.

Figure 10 shows the relations between depletion of Si and Mg scaled from δ(Fe) and log N(H) in the MW, LMC, SMC (solid lines); and IC 1613 and Sextans A (dashed lines). For Si, IC 1613 shows a similar relation to the LMC, while Sextans A has a similar slope but a different zero-point (as expected, since metals become less depleted with decreasing metallicity). For

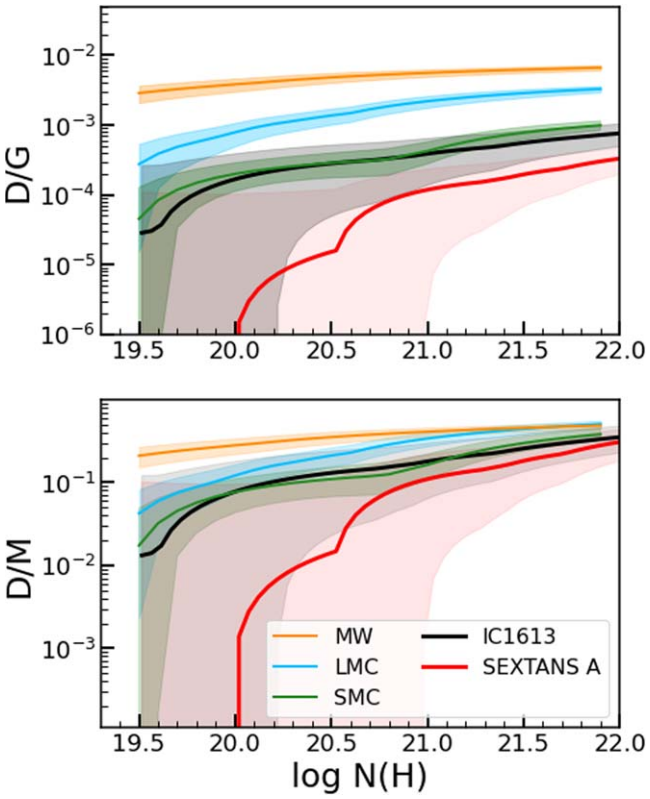

Figure 11. Dust-to-gas ratio (top) and dust-to-metal ratio (bottom) as a function of log N(H) in Sextans A (red), IC 1613 (black), the SMC (green), LMC (blue), and MW (orange). The transparent bands mark the 1σ uncertainty. The metallicity drops from solar at MW on the top to 10% solar with Sextans A at the bottom. D/M decreases with decreasing density and metallicity. As a result, D/G decreases faster than metallicity. IC 1613 and SMC, which have similar metallicities, have comparable D/G-ratios.

Mg, the extrapolated relation for METAL-Z galaxies has different slopes from the MW, LMC, and SMC. This difference arises from the slight slope variations between the LMC and MW relations between δ(Mg) and log N(H). Si is not as affected because the relation between δ(Si) and δ(Fe) has an almost identical slope in the MW and LMC. This example shows how subtle differences between elements can be amplified under our assumptions.

With the δ(X)–log N(H) relations in hand, we can sum the contributions of different elements to estimate D/G and D/M using Equations (8) and (9).

We remind the reader of two caveats. First, depletions for O and C have never been observed outside the MW. Therefore, the variations of the contributions of these two elements to the dust mass and composition with metallicity are uncertain. This limitation constitutes a source of significant systematic uncertainty in our D/G estimates, particularly because C and O constitute the main reservoir of metal mass in the ISM. Second, the relative invariance of the relation between the depletion of different elements with metallicity has never been tested below SMC metallicity (except for Fe and S, see Section 4.1).

5.2. *The Variations of* D/G *and* D/M *with Metallicity and Gas Density*

We show the evolution of D/G and D/M with gas column density (log N(H)) in Figure 11. We compare the relation between D/G (resp. D/M) and gas column density in the MW, LMC, SMC, IC 1613, and Sextans A in the top (resp. bottom) panel of Figure 11.

Table 9
D/G and D/M Measurements for Different Gas Column Densities in IC 1613 and Sextans A

	IC 1613		Sextans A	
log N(H) ($\mathrm{cm^{-2}}$)	(D/G)	(D/M)	(D/G)	(D/M)
20.3 [a]	$(2.26 \pm 2.23) \times 10^{-4}$	0.10 ± 0.10	$(0.12 \pm 1.02) \times 10^{-4}$	0.01 ± 0.09
21	$(3.81 \pm 2.50) \times 10^{-4}$	0.18 ± 0.12	$(1.15 \pm 1.14) \times 10^{-4}$	0.11 ± 0.11
22	$(7.56 \pm 2.69) \times 10^{-4}$	0.35 ± 0.12	$(3.28 \pm 1.36) \times 10^{-4}$	0.30 ± 0.13

Note.
[a] D/G and D/M at the lowest measured gas column density, log $N(\mathrm{H}) = 20.26\,\mathrm{cm^{-2}}$ for IC 1613, and log $N(\mathrm{H}) = 20.38\,\mathrm{cm^{-2}}$ for Sextans A.

D/M decreases with decreasing gas density and metallicity. In addition, the variation of D/M with gas density is substantially steeper at low metallicity than at solar metallicity. For example, D/M varies from 0.52 down to 0.3, or a factor of 1.7, in the MW between log $N(\mathrm{H}) = 22\,\mathrm{cm^{-2}}$ and log $N(\mathrm{H}) = 20\,\mathrm{cm^{-2}}$ (Roman-Duval et al. 2022a). For IC 1613 and Sextans A, where we do not have measurements down to log $N(\mathrm{H}) = 20\,\mathrm{cm^{-2}}$, we quote the D/G and D/M at the lowest measured column density log $N(\mathrm{H}) = 20.3\,\mathrm{cm^{-2}}$. In Sextans A, at 10% solar metallicity, D/M decreases from 0.30 at log $N(\mathrm{H}) = 22\,\mathrm{cm^{-2}}$ to 0.01 at the lowest log N(H) probed by the sample, or $20.3\,\mathrm{cm^{-2}}$ (factor of 30 decrease). In IC 1613, which has ~15% solar metallicity, D/M decreases from 0.35 to 0.10, or a factor of 3, over log $N(\mathrm{H}) = 22$ to $20.3\,\mathrm{cm^{-2}}$ (see Table 9).

From the variations reported in Figure 11 and in Table 9, as well as those reported in Table 4 of Roman-Duval et al. (2022a), it is also evident that the zero-point of D/M for a given column density also decreases with decreasing metallicity. At the highest column densities (log $N(\mathrm{H}) = 22\,\mathrm{cm^{-2}}$), D/M in Sextans A is 1.7 times lower than in the MW, while, in the diffuse ISM (log $N(\mathrm{H}) = 20.3\,\mathrm{cm^{-2}}$), D/M in Sextans A is 30 times lower than in the MW.

The steeper variations of D/M with gas density at lower metallicity stem from the combination of two effects. First, the fraction of an element in dust is given by $(1–10^{\delta(\mathrm{X})})$, and the function $y(x)=(1–10^{x})$ takes a steep downturn when x approaches zero from negative values. As a result, the fraction of X in dust varies from 0% to 50% between depletion values of 0 and −0.3. Second, as the metallicity decreases, the zero-point of the depletions becomes less negative (i.e., metals are less depleted). As a result, the gas column density at which elements become undepleted ($\delta(\mathrm{X}) = 0$) moves to higher values as the metallicity decreases (see the location of the kinks in Figure 8 moving to the right as the galaxy metallicity decreases). The combination of these two effects leads to the fraction of various elements in dust, and therefore D/M, dropping steeply over an increasingly wide range of gas column densities as the metallicity decreases. The direct consequence of this effect is that, at low metallicity, the variations of D/M, and subsequently D/G, over the range of gas column densities between log $N(\mathrm{H}) = 20$ and $22\,\mathrm{cm^{-2}}$

can be significantly larger than at higher metallicity, as illustrated in Figure 11.

Because D/G is the product of metallicity and D/M, the variations of D/M with gas density and metallicity observed in the bottom panel of Figure 11 are reflected in the variations of D/G seen in the top panel, with the additional imprint of the large metallicity changes between galaxies in the sample (i.e., from Sextans A at ∼10% solar metallicity to the MW). The variations in D/G with gas density are larger at low metallicity than at solar metallicity (similar to variations in the D/M). And because D/M decreases with decreasing metallicity, the D/G decreases faster than metallicity. At the extreme end of log $N(\mathrm{H}) = 20.3\ \mathrm{cm}^{-2}$, D/G in Sextans A (0.12×10^{-4}, Table 9) is over 300 times lower than in the MW (3.83×10^{-3}, see Roman-Duval et al. 2022a). At the higher column density end, this difference is reduced to a factor of 20 (3.28×10^{-4} in Sextans A versus 6.74×10^{-3} in the MW).

The increase in D/M and correspondingly D/G with gas density for a fixed metallicity results from the evolution of the steady-state equilibrium abundance between, on the one hand, the dust formation in stellar sources (asymptotic branch stars, supernovae, hereafter SNe) and dust growth in the ISM through the accretion of gas-phase metals onto dust grains and, on the other hand, the dust destruction by SN shocks and dust dilution by pristine inflows. The timescale for dust growth is inversely proportional to gas density (Asano et al. 2013; Feldmann 2015; Zhukovska et al. 2016). In turn, the timescale for dust destruction by SN shocks increases as the gas density increases, because SN shocks cannot propagate at high speeds in a dense medium, and because dust destruction only occurs at speeds $> 50\ \mathrm{km\ s}^{-1}$ (Jones et al. 1996). As a result, the D/M and D/G, which result from the steady-state balance between dust growth and destruction, increase with increasing gas density.

In addition, because D/M is lower in low-metallicity galaxies than in the MW, with an even more pronounced difference in the diffuse ISM, there are more metals in the gas phase available to accrete onto dust grains in those environments. This larger reservoir of potential dust components in the gas results in a steeper and wider variation of the D/M and D/G from the diffuse to dense ISM, where a significant fraction of the gas-phase metals have accreted onto dust grains.

5.3. Variations of D/G with Metallicity: Comparison of Different Observational Constraints

In Figure 12, we present a comparison of the evolution of D/G with metallicity between chemical evolution models (Feldmann 2015) and different observational estimates of D/G: depletions derived from UV spectroscopy in nearby galaxies (this work for IC 1613 and Sextans A; Roman-Duval et al. 2022a, and references therein for the MW, LMC, SMC); FIR + 21 cm + CO (1-0) emission maps of nearby galaxies (Rémy-Ruyer et al. 2014; De Vis et al. 2019); depletions derived from rest-frame UV spectroscopy and calibrations of abundance ratios in DLAs (De Cia et al. 2016; Quiret et al. 2016; Péroux & Howk 2020; Roman-Duval et al. 2022b).

D/G estimates from depletions in the MW, LMC, and SMC (Roman-Duval et al. 2022a) and this work (IC 1613 and Sextans A) are plotted for different log $N(\mathrm{H})$ values (log $N(\mathrm{H}) = 20, 21, 22\ \mathrm{cm}^{-2}$ in Figure 12.

Theoretical models from Feldmann (2015, gray) are also shown in Figure 12, and predict a turnover and steep decrease in the D/G-ratio below a critical metallicity of $Z < 0.1$–$0.2\ Z_{\odot}$. In the model, the critical metallicity is determined by the ratio γ of the timescale for the depletion of molecular gas by star formation, or about 2–4 Gyr (Bigiel et al. 2008), to the timescale for dust growth in the ISM at solar metallicity and densities of $100\ \mathrm{cm}^{-3}$, or about 1.5×10^5 yr (Hirashita 2000; Feldmann 2015). For a fiducial parameter $\gamma = 3 \times 10^4$, the critical metallicity is about 10% solar. This critical metallicity marks a transition point where dust growth in the ISM becomes insufficient to counterbalance the effects of dust destruction in SN shocks and dilution through gas inflows. As a result, the D/G below the critical metallicity is driven by stellar inputs of dust (evolved stars, SNe), resulting in a low D/M and D/G. Combining D/G measurements across a wide range of metallicities allows us to test the theoretically predicted D/G-ratio dependence on metallicity.

The most extensive sample of D/G measurements comes from FIR dust emission (Rémy-Ruyer et al. 2014; De Vis et al. 2019, dark blue points). We also show recent FIR measurements of D/G in the LMC and SMC (Clark et al. 2023) at log $N(\mathrm{H}) = 21\ \mathrm{cm}^{-2}$ (blue stars), as well as IC 1613 (Nersesian et al. 2019) and Sextans A (Shi et al. 2014). The mean hydrogen column densities over the apertures used for the FIR-based D/G measurements in IC 1613 and Sextans A are $4.04 \times 10^{20}\ \mathrm{cm}^{-2}$ and $1.4 \times 10^{21}\ \mathrm{cm}^{-2}$, respectively. The dust surface density is derived from FIR emission, while the atomic gas and molecular gas surface densities are traced by 21 cm and CO rotational emission, respectively. FIR measurements for $Z > 0.1\ Z_{\odot}$ show a significant scatter around the linear relation between D/G and metallicity. At lower metallicities, FIR-based D/G measurements mostly follow the model-predicted steep turnover in D/G for $\gamma \sim 3 \times 10^4$. However, the resolved FIR measurements in IC 1613 and Sextans A tend to lie on the upper envelope of the scatter in this trend.

In DLAs, only gas-phase abundances can be measured, and stellar abundances are not known. In this case, depletions are therefore derived from the [Zn/Fe] abundance ratio tied to a calibration of δ(Zn) versus [Zn/Fe] in the MW, LMC, or SMC (De Cia et al. 2016; Roman-Duval et al. 2022b). The depletion-based estimates of D/G in DLAs (De Cia et al. 2016; Quiret et al. 2016; Roman-Duval et al. 2022b) follow a slightly sublinear relation with metallicity, even below 10% solar. As a result, the trend of D/G versus metallicity seen in DLAs lies significantly higher than the trend derived from FIR + 21 cm + CO measurements in nearby galaxies from the Rémy-Ruyer et al. (2014), Nersesian et al. (2019) samples. However, the resolved FIR measurements in IC 1613 and Sextans A are in good agreement with the trend obtained in DLAs. In addition, the D/G estimates in DLAs are higher than the predictions from the Feldmann (2015) chemical evolution model with a fiducial γ parameter of 3×10^4. The trend of D/G versus metallicity in DLAs suggests very high values of γ, of the order 10^6 (left edge of the gray tracks in Figure 12). This implies a very fast dust growth timescale compared to the star formation timescale.

At high metallicity (above 10% solar, which includes IC 1613), the model and observed trends of D/G versus metallicity generally agree between all tracers and systems (FIR in nearby galaxies, UV spectroscopic depletions in nearby galaxies, and rest-frame UV spectroscopy in DLAs). We do note the factor of 3–4 discrepancy between the resolved FIR-based (Clark et al. 2023) and depletion-based (Roman-Duval et al. 2022a) D/G in the SMC, however, which might be due to a combination of factors examined later in this section.

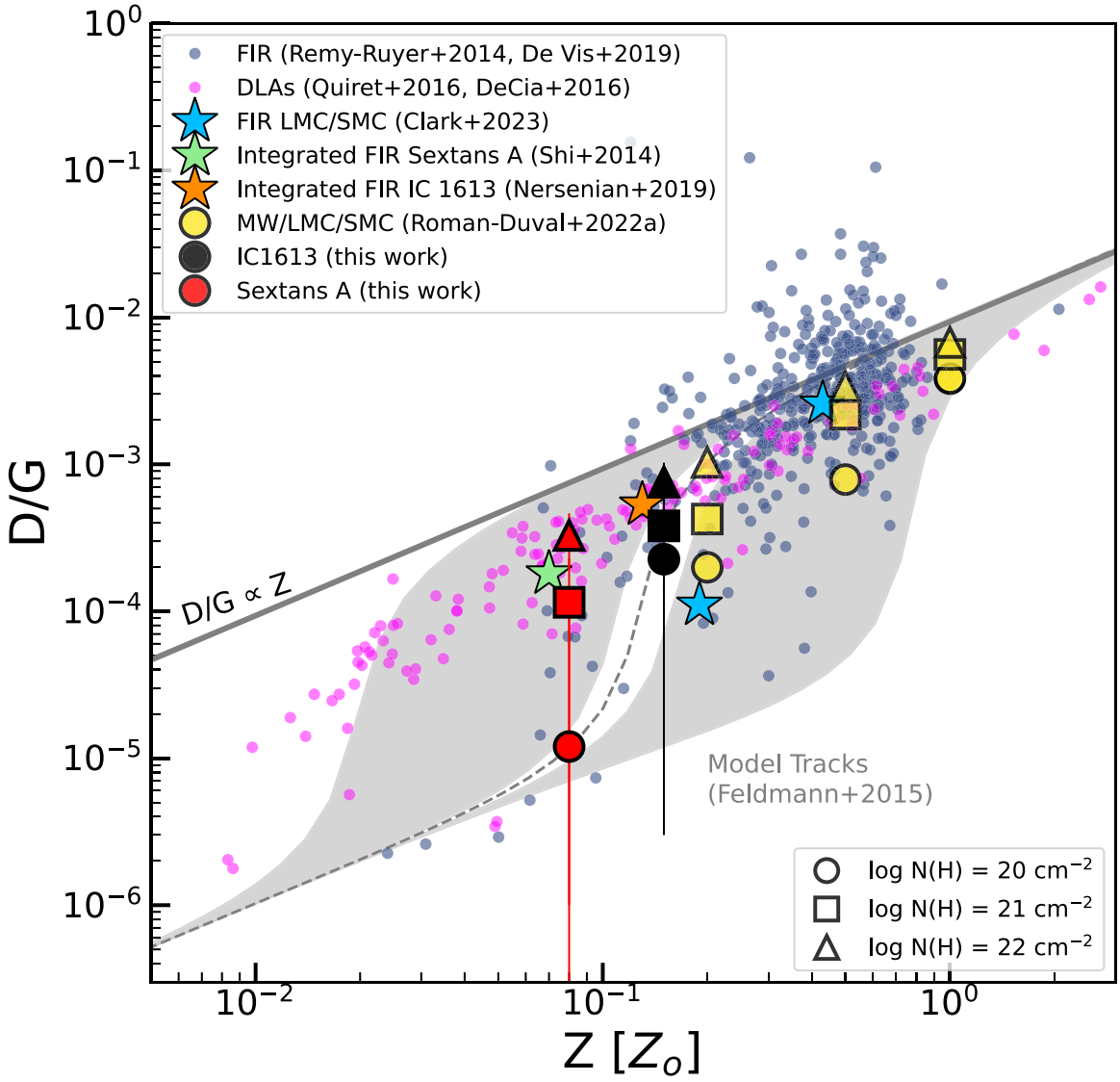

Figure 12. Dust-to-gas mass ratio as a function of (total) metallicity for different samples and types of observations. The dark blue points correspond to FIR emission measurements in nearby galaxies from Rémy-Ruyer et al. (2014), De Vis et al. (2019), LMC/SMC (Clark et al. 2023), IC 1613 (Nersesian et al. 2019), and Sextans A (Shi et al. 2014). The mean hydrogen column densities over the apertures used for the FIR-based D/G measurements in IC 1613 and Sextans A are 4.04×10^{20} cm^{-2} and 1.4×10^{21} cm^{-2}, respectively. In magenta are D/G estimates in DLAs from De Cia et al. (2016), Quiret et al. (2016). Dust depletion measurements from this work (IC 1613 in black, Sextans A in red) and from the literature (MW, LMC, SMC in yellow; Roman-Duval et al. 2022a) are shown as symbols for three hydrogen column density values: log N(H) = 20 cm^{-2} (circle), 21 cm^{-2} (square), and 22 cm^{-2} (triangle). Lastly, the gray shaded area shows the chemical evolution model from Feldmann (2015) for a range of γ parameters ($2 \times 10^3 - 10^6$). The dashed black line represents the fiducial $\gamma = 3 \times 10^4$ model, in best agreement with the trend obtained from FIR measurements. A solid gray line marks the linear relation between D/G and metallicity.

At metallicities below 10% solar (i.e., in Sextans A), the trend of D/G versus metallicity obtained from depletions lies in excellent agreement with the trend seen in DLAs for column densities log N(H) = 21–22 cm^{-2}. The FIR-based resolved D/G measurement in Sextans A, which was derived in an aperture where the gas column density is about 1.4×10^{21} cm^{-2}, is also in excellent agreement with the depletion-based measurement for those gas column densities. However, at hydrogen column densities of log N(H) ~20 cm^{-2}, the depletion-based D/G estimate in Sextans A lies almost perfectly on the trend of D/G versus metallicity obtained from the large sample of FIR measurements (Rémy-Ruyer et al. 2014; De Vis et al. 2019), a significant fraction of which are unresolved.

In a nutshell, there is a general tension between two types of constraints for the trend of D/G versus metallicity: from large samples of FIR measurements in nearby galaxies on the one hand, which suggest a steep drop in D/M and D/G at a critical metallicity of about 20% solar; and from rest-frame UV spectroscopy, both in local and high-redshift systems on the other hand, which suggest a slightly sublinear relation between D/G and metallicity, but do not exhibit any such steep drop in D/G below 10% solar metallicity. There are, however, exceptions to this discrepancy: the resolved FIR measurements of D/G in Sextans A at 7% solar metallicity lie on top of the trend derived from DLAs, and are in excellent agreement with the depletion-based D/G estimates for log N(H) > 21 cm^{-2}; conversely, the depletion-based D/G estimates for log N(H) ~20 cm^{-2} in Sextans A lie on top of the trend of D/G versus metallicity obtained from large samples of FIR measurements.

Chemical evolution models can be tuned to match both trends by adjusting the ratio of the timescale for the consumption of molecular gas by star formation to the timescale for dust growth in the ISM. The γ value in best agreement with the trend observed in the FIR is $\gamma \sim 3 \times 10^4$, while the trend seen from depletions is consistent with $\gamma = 10^6$, suggesting a much faster dust growth timescale compared to the gas consumption by star formation. In this case, dust could keep growing in low-metallicity environments.

A few culprits could explain the tension between FIR-based and UV-spectroscopy-based estimates of the trend of D/G versus metallicity, and the occasional discrepancy between D/G estimates from depletions and the FIR for a given galaxy (e.g., the SMC). As pointed out in Roman-Duval et al. (2022b), the conversion of FIR emission to dust mass relies on an assumed FIR opacity, which is only constrained observationally in the MW and has been shown from models and laboratory studies to depend on the composition, size, and fractal aspect of dust grains (e.g., Demyk et al. 2017b). However, this FIR opacity is unconstrained observationally and may well vary significantly with metallicity and density, since there is strong evidence that the composition, grain size, and optical properties of dust change significantly within and between galaxies. Examples of such evidence include studies based on the FIR (M31, M33, M101, M74, M83, and other nearby galaxies see Fritz et al. 2012; Smith et al. 2012; Chiang et al. 2018; Relaño et al. 2018; Clark et al. 2019; Lamperti et al. 2019), UV dust extinction curves in the Magellanic Clouds (Gordon et al. 2003), and depletion studies in the Magellanic Clouds (Roman-Duval et al. 2022a).

Furthermore, many 21 cm and FIR observations involved in the determination of the D/G in the Rémy-Ruyer et al. (2014), De Vis et al. (2019) samples either are unresolved or do not have aperture matching between the dust mass and gas mass estimates. It is, therefore, entirely possible that the D/G estimates obtained with this method may be underestimated due to the dilution of the dust mass in a larger, diffuse gas volume of low average column density. In this scenario, the steep variations of D/G with gas density at low metallicity, such as the one seen from depletions in Sextans A, could be playing a role in the apparent discrepancy between the trend of D/G versus metallicity derived from FIR and from depletions in nearby galaxies and DLAs. In particular, the unresolved measurements in galaxies where the dust disk could likely occupy a smaller volume than the gas disk could well be affected by a dilution of the dust component in the larger diffuse gas component, resulting in an artificially low D/G estimate (corresponding to a low average gas column density).

The D/G estimate from UV-spectroscopy is not immune to systematics either. As mentioned earlier in this paper, the large contribution of C and O to the dust budget is highly uncertain owing to the sparsity and uncertainties of C measurements in the MW and the lack of C and O depletion measurements altogether outside of the MW. It is entirely possible that variations in nucleosynthetic histories, particularly with metallicity, could lead to varying abundance ratios and chemical affinities for dust grains. This would result in departures in the relation between Fe depletions and depletions of other elements from the MW relations. This could lead to large (but not quantifiable) systematic uncertainties in D/G estimates based on depletions.

Nevertheless, the METAL-Z large Hubble program shows the potential for depletion measurements in low-metallicity systems to help resolve the tension between D/G estimates from the FIR and from spectroscopy of DLAs. Depletion measurements in nearby low-metallicity galaxies where both interstellar and stellar abundances can be measured can be especially impactful for these calibrations as DLAs are often used to trace the metal enrichment at higher redshift, where low-metallicity systems are more common. Additional measurements in Sextans A and other low-metallicity dwarfs in the Local Group alongside robust stellar abundances will further constrain relations between elemental depletion and dust-to-gas ratio, deepening our understanding of dust at metallicity below 20% solar.

6. Conclusions

We presented the results of the METAL-Z Hubble program targeting 18 sight lines toward massive stars in two local low-metallicity dwarf galaxies, IC 1613 (10% solar oxygen metallicity, 20% solar iron metallicity) and Sextans A (10% solar metallicity). We used COS FUV spectroscopy toward those massive stars to measure gas-phase column densities of hydrogen, iron, and sulfur and, in turn, calculate the gas-phase abundances and elemental depletion of Fe and S.

The relation between the depletions of Fe and S in IC 1613 and Sextans A is consistent within errors with the relations between these elements established in the MW, LMC, and SMC.

Similarly to findings in the MW, LMC, and SMC, the depletions of Fe in IC 1613 and Sextans A show a declining trend with increasing gas column density, indicating that the fraction of Fe locked in dust increases when the gas density of the ISM increases due to dust growth in the ISM through the accretion of gas-phase metals onto dust grains. We also found that the base level of Fe depletion increases with decreasing metallicity. At $\log N(\mathrm{H}) = 21\,\mathrm{cm}^{-2}$, the Fe depletion value increases by 0.55 dex from the MW to IC 1613 and by 0.85 dex from the MW to Sextans A. This corresponds to a reduction of the fraction of Fe in dust from 0.97 to 0.81 between the MW and Sextans A at $\log N(\mathrm{H}) = 21\,\mathrm{cm}^{-2}$, and implies that metals become less depleted from the gas as the metallicity of a galaxy decreases. At lower column densities ($\log N(\mathrm{H}) = 20.3\,\mathrm{cm}^{-2}$), the reduction in the fraction of Fe in dust from the MW to Sextans A is even more dramatic, going from 0.97 to 0.32 (the fraction of Fe in dust decreases from 0.97 in MW to 0.74 in IC 1613 at this column density).

To estimate the depletions of other, unobserved metals, we used the relation between the depletion of Fe and the depletion of other elements measured in the MW, where abundances and depletions for a complete set of elements can be obtained. This assumption is based on the findings that (1) the relation between the depletions between various elements appears relatively invariant with metallicity in the MW, LMC, and SMC, and (2) the relation between the depletions of Fe and S in IC 1613 and Sextans A is consistent with that found in the MW, LMC, and SMC. The caveat to this assumption is twofold. First, the depletions of C and O, which are major mass reservoirs of metals for dust, have never been measured outside the MW. Given that the stellar C/O ratio in low-metallicity galaxies tends to be lower than in the MW, the chemical affinities of dust grains could change in low-metallicity systems, which would result in a different relationship between

the C or O depletion and the depletion of Fe at low metallicity. Second, the metallicity invariance of the relation between the depletions of different elements has not been tested at metallicities lower than that of the SMC (20% solar), other than for Fe and S (this work). Nevertheless, this assumption allows us to estimate the dust-to-gas and dust-to-metal ratios from the depletions of Fe measured in IC 1613 and Sextans A.

Based on the fundamental assumption that the depletions of Fe and other elements in Sextans A and IC 1613 follow the same relations as in the MW, we estimate the depletions of all constituents of dust as a function of log N(H) and derive the dust-to-gas and dust-to-metal ratios in IC 1613 and Sextans A, as a function of log N(H). As indicated by the trends obtained from Fe alone, we find that D/M increases with increasing column density, by factors of 3.5 and 35 in IC 1613 and Sextans A, respectively, between log $N(\mathrm{H}) = 20.3$ and 22 cm^{-2}. These variations imply that dust growth does occur at low metallicity, resulting in significant changes in the dust abundance with the ISM density.

In addition, D/M decreases with decreasing metallicity for a given gas column density, from 0.41 ± 0.5 in the MW at log $N(\mathrm{H}) = 21\ \mathrm{cm}^{-2}$ to 0.28 ± 0.12 in IC 1613 and to 0.19 ± 0.13 in Sextans A at the same column density. The variation of D/M with metallicity is more pronounced at a lower column density, with a factor of 40 variation from the MW to Sextans A at log $N(\mathrm{H}) = 20\ \mathrm{cm}^{-2}$. As a result of the varying D/M, D/G decreases slightly faster than metallicity (but not as fast as observed in the FIR).

We compare the evolution of D/G with metallicity derived from depletion-based estimates in this work (Sextans A, IC 1613) and previous work (SMC, LMC, MW) with D/G estimates obtained from two different techniques and samples: (1) a combination of FIR emission to trace dust and 21 cm + CO rotational emission to trace atomic and molecular gas; and (2) spectroscopic measurements of the [Zn/Fe] abundance ratio in DLAs, from which D/G can be estimated using calibrations derived in the MW (De Cia et al. 2016). At metallicities below 20% solar, the depletion-based measurements in Sextans A and IC 1613 are in good agreement with the trend obtained in DLAs, which is only slightly sublinear with metallicity. Conversely, the trend obtained from FIR observations sees a steep decline of D/M and D/G below 20% solar metallicity, which is not observed from depletions in nearby galaxies and DLAs. This solidifies the tension between the trends of D/G versus metallicity derived from FIR in nearby galaxies on the one hand and rest-frame UV spectroscopy in nearby galaxies and DLAs on the other hand.

Constraining the dust abundance and the dust-to-gas ratio in low-metallicity environments is crucial for understanding the ISM of galaxies and chemical enrichment across cosmic time. With this work, we showed that depletion measurements based on UV spectroscopy are a powerful tool for estimating the abundance of dust at low metallicity. In the future, we will expand the studies to more galaxies, constraining the dust abundances in a broad range of metallicity and gas density environments.

Acknowledgments

A.H., E.B.J., and K.T. acknowledge support from grant No. HST-GO-15880. This work is based on observations with the NASA/ESA Hubble Space Telescope obtained at the Space Telescope Science Institute, which is operated by the Associations of Universities for Research in Astronomy, Incorporated, under NASA contract NAS5-26555. These observations are associated with program 15880. Support for program No. 15880 was provided by NASA through a grant from the Space Telescope Science Institute, which is operated by the Association of Universities for Research in Astronomy, Incorporated, under NASA contract NAS5-26555. M.G. acknowledges support by grants PID2019-105552RB-C41, PID2022-137779OB-C41, PID2022-140483NB-C22, and MDM-2017-0737 Unidad de Excelencia "Maria de Maeztu"—Centro de Astrobiologia (CSIC-INTA), funded by MCIN/AEI/10.13039/501100011033. The HST data presented in this article were obtained from the Mikulski Archive for Space Telescopes (MAST) at the Space Telescope Science Institute. The specific observations analyzed can be accessed via DOI:10.17909/1hzc-8k61.

Appendix A
Metal Column Densities Measured with Curve of Growth

In this appendix, we provide an overview of our metal line column density measurements achieved by utilizing the Curve of Growth (CoG) method. The CoG method is a classical and widely used approach for determining column densities of absorption lines. Nevertheless, our analysis reveals that, when applied to the low S/N COS spectra of the METAL-Z sample, this method proves insufficient in yielding conclusive measurements.

A.1. Equivalent Width Measurements

The CoG method uses equivalent widths of the lines to calculate the column density of the ion. To measure equivalent widths, we first had to determine the integration limits for each line. We assumed that all ISM lines have the same velocity dispersion toward a given sight line. We then used the S II λ1253 Å (IC 1613) or 21 cm HI profile toward a particular sight line (Sextans A, from LITTLE-THINGS survey; Ott et al. 2012) to determine the velocity integration limits and then apply those limits to all lines. We chose S II λ1253 Å as it is a medium-strength isolated line, for which our approach worked best. However, for Sextans A, where all metal lines are weaker (due to the lower abundance), we found that using the strong 21 cm H I line provides the most optimal results.

We designed a method to determine integration limits in an objective, automated, and reproducible process. First, we calculated the derivative of the S II λ1253 Å (or 21 cm H I) line equivalent width as a function of the distance from the line center. The resulting derivative curve grows from the center of the line outwards until it starts to plateau, indicating that the flux has reached the continuum level. We fit a Gaussian function to the derivative curve for each sight line and use 4σ to mark the place where the line recovers to the continuum. We found that the 3σ cutoff underestimates the contribution from line wings, while 5σ often incorporates wings of neighboring lines. Therefore, we settled with 4σ as the most robust representation of the limit between the line and continuum dominant contribution to the equivalent width measurement.

Once integration limits are determined for all sight lines, we can proceed with equivalent width measurements for S and Fe lines. We measured three Fe II lines: Fe II $\lambda\lambda\lambda$ 1142, 1143, 1144 Å, (see Figure 13 and Table 3). For four sight lines covered by the G160M, λ1608 Å was also available, and we included it in the measurements. The short wavelength part of the spectrum

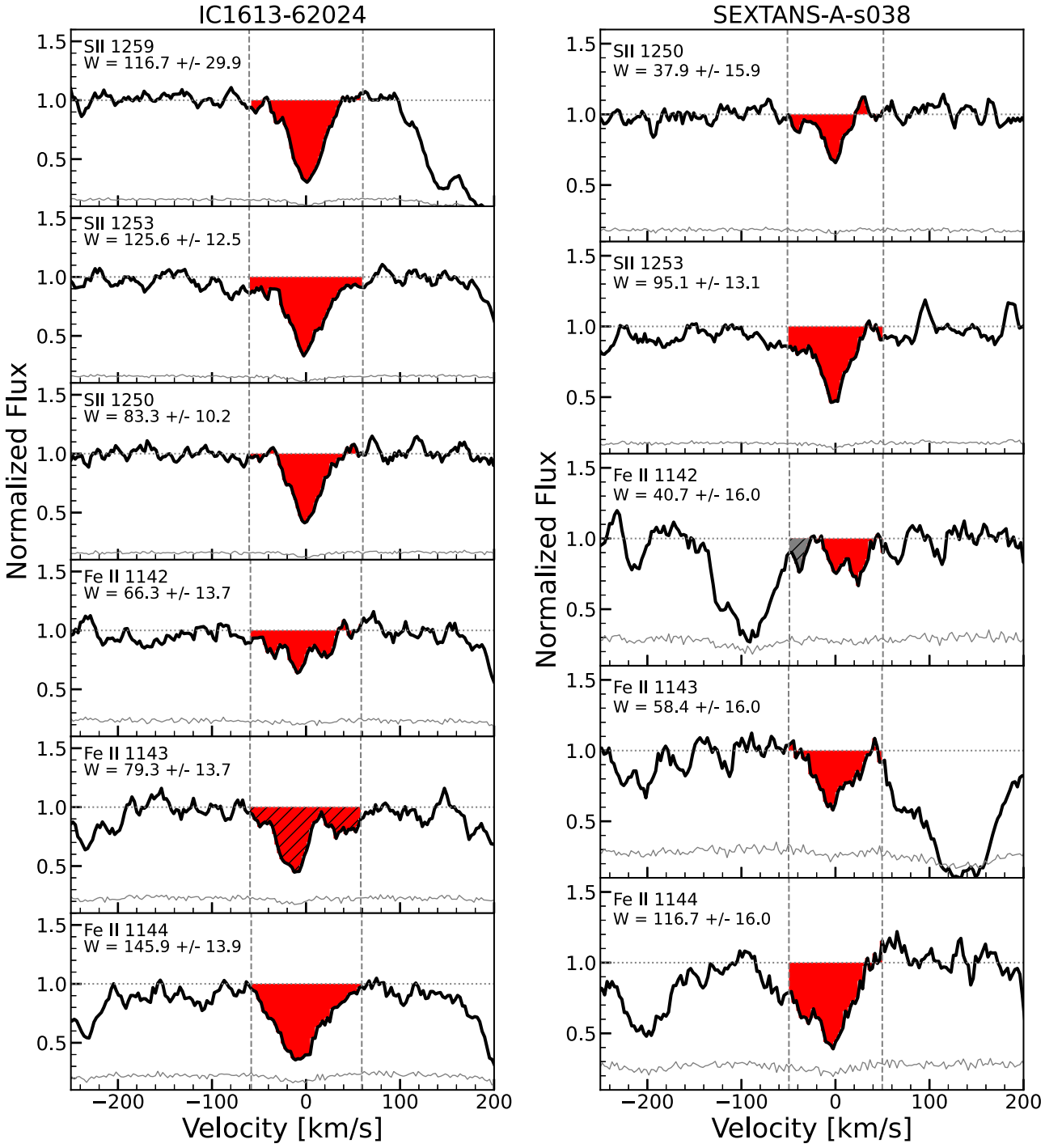

Figure 13. Examples of line measurements for selected sight lines in IC 1613 and Sextans A. We show all lines used for abundance measurements. In black, we plot smoothed, continuum-subtracted spectra centered at the line in the velocity frame of the particular galaxy. Dashed vertical lines mark the equivalent width integration limits, while the red fill shows the whole integration range. In IC 1613, Fe II λ1143 Å line is completely blended with MW Fe II λ1142 Å line and is hatched (see Appendix A.1 for full discussion). For Sextans A, we do not show S II λ1259 Å as it is contaminated by an MW line. In gray, we mark contaminated line regions excluded from the measurements.

proved challenging due to the dropping sensitivity of COS. Therefore, for ten sight lines, the weak Fe II λ1142 Å line remains undetected, and we report upper limits on the equivalent width. In Sextans A, the Fe II λ1142 Å line is slightly blended with the MW's Fe II λ1143 Å line. For equivalent width measurements of this line, we had to manually mask the contaminated part of the line within automatically selected velocity limits (the masked region is marked in Figure 13).

Due to the velocity difference between IC 1613 and the MW, the Fe II λ1143 Å line originating from IC 1613 completely blends with the MW's Fe II λ1142 Å line. As we cannot disentangle them from profile shapes, we used other Fe II lines originating from the MW to estimate the equivalent width of the blended MW λ1142 Å line. Specifically, we measured the equivalent width of the λ1143 and λ1144 Å MW lines and fitted a CoG (details of the method in Appendix A.2). We

Table 10
Equivalent Width Measurements of Fe II and S II Lines in METAL-Z Targets

Sight Line	Ion	λ (Å)	W_λ (mÅ)	$v_{\rm limit}$[a] (km s^{-1})	LSF[b] (%)
IC1613-61331	S II	1250.578	66.21 ± 8.95	52	4
IC1613-61331	S II	1253.805	157.81 ± 13.01	52	4
IC1613-61331	S II	1259.518	108.70 ± 27.18	52	4
IC1613-61331	Fe II	1142.366	8.40 ± 11.30	52	5
IC1613-61331	Fe II	1143.226	67.10 ± 11.30	52	5
IC1613-61331	Fe II	1144.938	108.82 ± 11.45	52	5
IC1613-62024	S II	1250.578	83.30 ± 10.22	60	3
IC1613-62024	S II	1253.805	125.57 ± 12.50	60	3
IC1613-62024	S II	1259.518	116.72 ± 29.91	60	3
IC1613-62024	Fe II	1142.366	66.32 ± 13.73	60	3

Notes.
[a] The velocity limits used for the equivalent width calculations.
[b] The fraction of missing flux due to the LSF wings outside of the equivalent width integration limits.

(This table is available in its entirety in machine-readable form.)

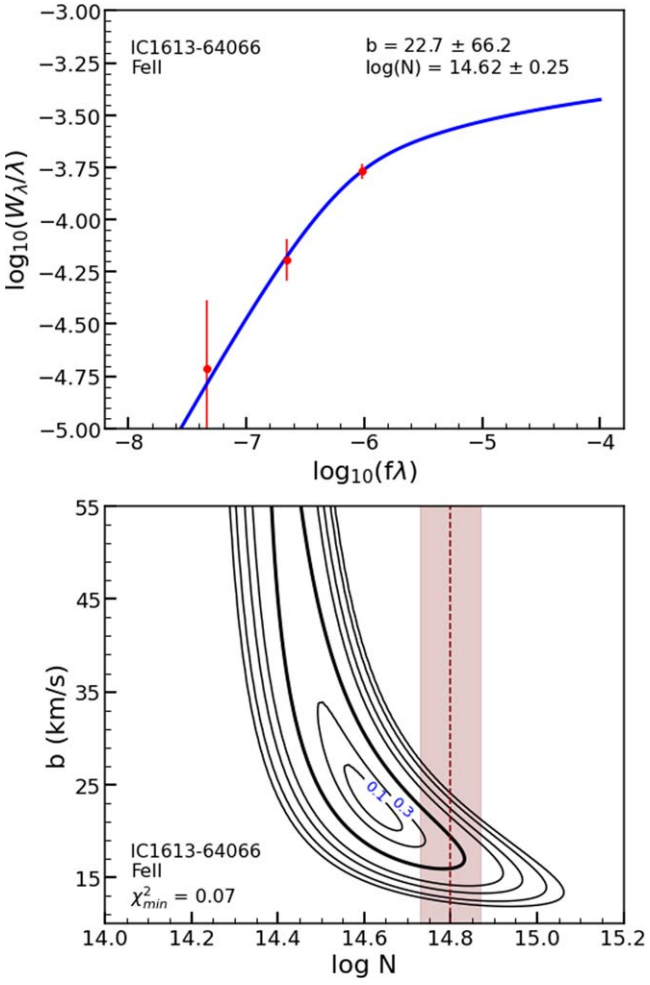

Figure 14. Curve of growth model best-fit parameters and probability contours. The top panel shows the best-fitting model (blue curve) with measurements (red points) and corresponding parameters listed. The bottom panel displays the probability contours for the model's N and b parameters, with the 1σ contour highlighted in bold. Results from Voigt profile fitting are shown as the red band.

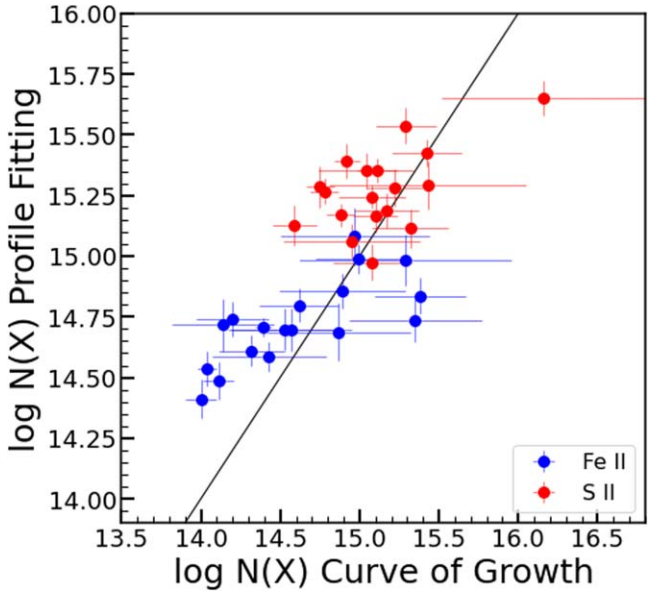

Figure 15. Comparison of column density measurements between curve of growth and profile fitting methods for Fe II (blue) and S II (red). A 1:1 line is marked in black; dashed lines mark the 1σ dispersion. Most measurements are similar within uncertainties, and the outliers have significant errors. Two measurement methods provide comparable results; we chose the curve of growth results for further analysis.

found that the blended Fe II λ1142 Å and λ1143 Å lines in both IC 1613 and MW are optically thin—they lay on the linear part of the CoG. In this regime, the equivalent width of blended lines equals the sum of their individual equivalent widths. Therefore, we estimated the equivalent width of the IC 1613's λ1143 Å line by subtracting the MW's λ1142 Å equivalent width from the one measured over the blended line. We summarize the measurements of equivalent width for all lines in the online materials, for which an excerpt is shown in Table 10. We present the measurements for each step of this procedure (equivalent widths of MW lines, blend, results of CoG, and derived Fe II λ1143 Å for IC 1613) in Table 11.

For the second measured element, S, we cover three S II lines: $\lambda\lambda\lambda$ 1250, 1253, 1259 Å. In Sextans A, the latter is blended with the stronger MW Si II λ1259 Å absorption line. Therefore, for that galaxy, we only report measurements for the S II λ1250 Å and λ1253 Å.

COS LSF have broad wings that can contain up to 30% of the observed flux (Roman-Duval et al. 2013). To test whether the limiting velocity selection influences our equivalent width measurement, we have integrated the LSF outside the line integration limits. We found that the fraction of missing flux ranges between 1% and 10% for most sight lines, well within the flux measurement uncertainty. The fractions of flux missing due to the LSF wings for each sight line can be found in Table 4, but it is not incorporated into the final measurements as it is smaller than the measurement errors.

A.2. Column Density Measurements with the Curve of Growth Method

In the CoG approach, for each element, we find the best-fitting model for the relation between observed equivalent width and oscillator strength f_λ of all measured lines. The

Table 11
Fe II Equivalent Width Derivation from Blended IC1613/1143 + MW/1142 Lines

Target	MW λ1144[a] (mÅ)	MW λ1143[b] (mÅ)	IC1613/λ1143 + MW/λ1142[c] (mÅ)	MW λ1142[d] (mÅ)	IC1613 λ1143[e] (mÅ)
IC1613-61331	180.47 ± 19.22	82.68 ± 14.71	68.79 ± 9.51	21.48 ± 11.66	47.31 ± 15.05
IC1613-62024	184.24 ± 18.82	80.53 ± 15.10	113.66 ± 14.33	20.64 ± 11.76	93.02 ± 18.54
IC1613-64066	163.44 ± 19.64	66.98 ± 15.85	89.38 ± 12.85	16.55 ± 11.66	72.82 ± 17.35
IC1613-67559	163.48 ± 18.55	79.92 ± 13.63	59.84 ± 11.28	21.70 ± 11.35	38.14 ± 16.00
IC1613-67684	161.79 ± 15.77	78.65 ± 14.14	39.11 ± 8.55	21.24 ± 11.34	17.88 ± 14.20
IC1613-A13	170.19 ± 19.28	78.78 ± 16.82	75.36 ± 12.36	20.49 ± 11.53	54.87 ± 16.91
IC1613-B11	178.22 ± 18.73	119.34 ± 16.32	42.31 ± 12.91	43.42 ± 11.10	> 17.03
IC1613-B2	164.71 ± 19.45	107.58 ± 20.78	126.40 ± 13.87	37.60 ± 10.95	88.80 ± 17.68
IC1613-B3	143.99 ± 16.64	42.72 ± 12.53	9.55 ± 12.26	9.39 ± 12.33	> 17.39
IC1613-B7	180.42 ± 23.93	75.16 ± 16.26	68.83 ± 11.84	18.55 ± 11.82	50.28 ± 16.73

Notes.
[a] Equivalent width of Fe II λ1144 from Milky Way.
[b] Equivalent width of Fe II λ1143 from Milky Way.
[c] Equivalent width of blended Fe II IC 1613 λ1143 + Milky Way λ1142.
[d] Equivalent width of Fe II λ1142 from Milky Way, derived through CoG.
[e] The deblended equivalent width of IC 1613 Fe II λ1143.

Table 12
Column Density and Depletion Measurements Derived Using Curve of Growth Method

Target	log N(H I)[a] (cm^{-2})	log N(S II) (cm^{-2})	b (km s^{-1})	log N(Fe II) (cm^{-2})	b (km s^{-1})	$\delta(S)$[b]	δ(Fe)[b]
IC1613-61331	20.84 ± 0.03	$15.11^{+0.14}_{-0.13}$	$21.0^{+\infty}_{-8}$	$14.43^{+0.28}_{-0.36}$	$12.0^{+\infty}_{-4}$	$-1.28^{+0.36}_{-0.28}$	$-0.13^{+0.13}_{-0.14}$
IC1613-62024	21.05 ± 0.03	$15.29^{+0.45}_{-0.19}$	12.0^{+8}_{-4}	$15.38^{+0.41}_{-0.29}$	9.0^{+2}_{-2}	$-0.54^{+0.29}_{-0.41}$	$-0.16^{+0.19}_{-0.45}$
IC1613-64066	20.88 ± 0.04	$15.42^{+0.92}_{-0.22}$	12.0^{+8}_{-5}	$14.62^{+0.20}_{-0.25}$	23.0^{+8}_{-5}	$-1.13^{+0.25}_{-0.20}$	$0.14^{+0.22}_{-0.92}$
IC1613-67559	20.47 ± 0.14	$15.10^{+0.17}_{-0.14}$	16.0^{+26}_{-6}	$14.32^{+0.30}_{-0.21}$	$22.0^{+\infty}_{-10}$	$-1.02^{+0.25}_{-0.33}$	$0.23^{+0.20}_{-0.22}$
IC1613-67684	20.44 ± 0.04	$15.08^{+0.19}_{-0.25}$	5.0^{+3}_{-5}	$14.04^{+0.35}_{-0.06}$	$20.0^{+\infty}_{-20}$	$-1.27^{+0.07}_{-0.35}$	$0.24^{+0.25}_{-0.19}$
IC1613-A13	20.26 ± 0.03	$15.32^{+1.36}_{-0.24}$	9.0^{+7}_{-4}	$14.57^{+0.39}_{-0.38}$	9.0^{+12}_{-3}	$-0.56^{+0.38}_{-0.39}$	$0.66^{+0.24}_{-1.36}$
IC1613- B11	20.37 ± 0.05	$15.17^{+0.36}_{-0.20}$	10.0^{+9}_{-4}	$14.00^{+0.47}_{-0.10}$	$20.0^{+\infty}_{-20}$	$-1.24^{+0.11}_{-0.47}$	$0.40^{+0.21}_{-0.36}$
IC1613-B2	21.17 ± 0.03	$16.16^{+3.74}_{-0.64}$	9.0^{+5}_{-4}	$14.99^{+0.32}_{-0.27}$	12.0^{+4}_{-3}	$-1.05^{+0.27}_{-0.32}$	$0.59^{+0.64}_{-3.75}$
IC1613-B3	20.64 ± 0.06	$15.22^{+0.27}_{-0.18}$	14.0^{+19}_{-5}	$14.11^{+0.22}_{-0.10}$	$20.0^{+\infty}_{-20}$	$-1.40^{+0.12}_{-0.23}$	$0.18^{+0.19}_{-0.28}$
IC1613-B7	20.73 ± 0.03	$15.08^{+0.36}_{-0.21}$	$17.0^{+\infty}_{-9}$	$14.39^{+0.22}_{-0.05}$	$20.0^{+\infty}_{-20}$	$-1.21^{+0.06}_{-0.22}$	$-0.05^{+0.21}_{-0.36}$
SEXTANS-A-s050	20.46 ± 0.04	$14.88^{+0.12}_{-0.09}$	$20.0^{+\infty}_{-20}$	$14.20^{+1.33}_{-0.23}$	$22.0^{+\infty}_{-17}$	$-0.81^{+0.23}_{-1.33}$	$0.43^{+0.10}_{-0.13}$
SEXTANS-A-s014	20.71 ± 0.03	$14.95^{+0.35}_{-0.43}$	$6.0^{+\infty}_{-6}$	$14.53^{+0.44}_{-0.36}$	8.0^{+11}_{-3}	$-0.73^{+0.36}_{-0.44}$	$0.25^{+0.43}_{-0.35}$
SEXTANS-A-s022	21.17 ± 0.03	$15.04^{+1.16}_{-0.30}$	$11.0^{+\infty}_{-6}$	$15.35^{+0.46}_{-0.42}$	5.0^{+1}_{-5}	$-0.37^{+0.42}_{-0.46}$	$-0.12^{+0.30}_{-1.16}$
SEXTANS-A-s038	21.11 ± 0.02	$14.78^{+0.39}_{-0.09}$	$20.0^{+\infty}_{-20}$	$14.89^{+0.57}_{-0.40}$	8.0^{+4}_{-3}	$-0.77^{+0.40}_{-0.57}$	$-0.32^{+0.09}_{-0.39}$
SEXTANS-A-s029	20.90 ± 0.07	$14.59^{+0.17}_{-0.14}$	$20.0^{+\infty}_{-20}$	$14.87^{+0.42}_{-0.45}$	5.0^{+2}_{-5}	$-0.58^{+0.46}_{-0.43}$	$-0.30^{+0.16}_{-0.18}$
SEXTANS-A-s037	21.11 ± 0.07	$14.75^{+0.17}_{-0.09}$	$20.0^{+\infty}_{-20}$	$14.97^{+0.43}_{-0.47}$	5.0^{+2}_{-5}	$-0.69^{+0.48}_{-0.44}$	$-0.35^{+0.11}_{-0.18}$
SEXTANS-A-SA2	21.07 ± 0.04	$14.92^{+0.36}_{-0.08}$	$20.0^{+\infty}_{-20}$	$15.29^{+0.58}_{-0.67}$	5.0^{+3}_{-5}	$-0.33^{+0.67}_{-0.58}$	$-0.14^{+0.09}_{-0.36}$
SEXTANS-A-s021	20.38 ± 0.04	$15.43^{+0.43}_{-0.62}$	5.0^{+14}_{-5}	$14.14^{+0.55}_{-0.32}$	$10.0^{+\infty}_{-5}$	$-0.79^{+0.32}_{-0.55}$	$1.06^{+0.62}_{-0.45}$

Notes.
[a] H I column density from Lyα profile fitting.
[b] Elemental depletion.

model is given by Equations (2)–(4) of Jenkins (1996) and links the line's equivalent width with the gas physical parameters: column density N and velocity dispersion b.

The central optical depth is defined as

$$\tau_0 = \frac{\pi^{1/2} e^2 f \lambda}{m_e c}\left(\frac{N}{b}\right). \quad \text{(A1)}$$

The equivalent width is defined as

$$\frac{W_\lambda}{\lambda} = \frac{2bF(\tau_0)}{c}, \quad \text{(A2)}$$

where

$$F(\tau_0) = \int_0^\infty [1 - \exp(-\tau_0 e^{-x^2})]\, dx. \quad \text{(A3)}$$

We created a grid of models with a range of (N, b) parameters $\log(N) = 10$–$20\ cm^{-2}$, with a spacing of $0.01\ cm^{-2}$, and $b = 5$–$100\ km\ s^{-1}$ with a spacing of $0.1\ km\ s^{-1}$. We then searched the grid for the best-fit model by minimizing the χ^2 between the model and the measured equivalent widths for the

different transitions. We calculate the χ^2 as

$$\chi^2_{ij} = \Sigma^N_{k=0} \frac{(w_k - m_{jk})^2}{s^2_k}, \quad \text{(A4)}$$

where w_k and s_k are the equivalent width measurements and associated errors for all lines for a given element, and m_{jk} is the model value of the equivalent width for a given N and b.

The model is best constrained for three or more measurements of a particular ion. In several cases, we only had two measurements (e.g., one of the S II lines in Sextans A were fully blended with an MW interloper), resulting in an unconstrained b. For these cases, we assumed $b = 20^{+\infty}_{-20}$ km s^{-1} (Table 12). The column density is less affected, and even with only two measurements, we could reasonably constrain N.

The CoG method is illustrated in Figure 14. In the top panel, we present the measurements of the equivalent widths of three Fe II lines as a function of the oscillator strength. The best-fit CoG model obtained by χ^2 minimalization is also shown.

To estimate the uncertainties on the best-fit parameters log (N) and b, we adopt the approach from Lampton et al. (1976), Roman-Duval et al. (2021). On the lower panel of Figure 14, we see the representation of probability contours in the (N, b) parameters' space. Following the Lampton et al. (1976) approach for two parameters, the contour of χ^2 corresponding to $\chi^2_{\rm min} + 2.3$ provides the 1σ uncertainties. The best-fit parameters (N, b) have the lowest value of χ^2, and we adopt them as the final measurement (Table 12).

In Figure 15, we present a comparison between the column density measurements obtained through the CoG method and the profile fitting method for two ions, S II (in red) and Fe II (in blue). To assess the agreement between the two methods, we include a 1:1 line in the plot and mark a 1σ dispersion with a dashed line. Most measurements agree with errors, with Fe column density measurements showing the largest discrepancies. The CoG method shows larger error bars, especially for Fe measurement, which are crucial for the analysis presented in this paper. While CoG provides results comparable to the profile fitting method, the constraints are insufficient for robust conclusions.

Appendix B
Testing the Forward Optical Depth Method

In this Appendix, we use "artificial absorption" tests to quantify the performance of the proposed forward optical depth (FOD) method. We take the ground truth component structures, synthesize the corresponding artificial spectra with noise properties representative of those in the sample, and use FOD to estimate total column densities. For comparison, we also estimate total column densities using Voigt profile fitting and the apparent optical depth (AOD) method. The first component structure is an Fe II absorption system taken from an analysis of a high-resolution (FWHM = 4 km s^{-1}) spectrum by Welty et al. (1997). This structure serves as a proof of concept, demonstrating that FOD can work on a realistic absorption system. The second component structure is a single Voigt profile with varying total column density We use this structure to characterize the performance of FOD at different absorption line depths.

Each set of tests is done at continuum noise levels chosen to represent the span of the real spectra analyzed in the main part of this work. We parameterize the noise level in terms of the *continuum photon rate* (CPR). This is a natural parameterization to use since the likelihood function used in the analysis operates on photon counts rather than on fluxes (see Section 3.3.1). The CPRs are 10 and 30, for Fe II, and 30 and 80, for S II. Note that these are CPRs for the intrinsic HST-COS pixel scale, not for a resolution element.

When creating a synthetic spectrum, we set the continuum and instrumental sensitivity (relative to a normalized spectrum) to 1. The expected number of photons μ at a pixel is then the CPR multiplied by the absorption spectrum at that pixel. μ is then used as the rate parameter for the Poisson distribution from which we draw an "observed" number of photons. We estimate a Gaussian flux uncertainty from the photon counts using the `poisson_conf_interval` function in `astropy` with the "frequentist-confidence" interval calculation method. This is how the photon count uncertainty is currently estimated in `calcos`.

The FOD implementation is similar to the one described in Section 3.3.3, the only change being that the velocity range is -100 to $+100$ km s^{-1}. Voigt profile fitting is implemented as a `numpyro` model with uniform component parameter priors between 12 and 18 for $\log_{10}(N/{\rm cm}^{-2})$, 2 and 60 for b, and -50 and 100 for the centroid. The model likelihood and continuum handling is the same as for FOD. AOD is done using a utility in the `linetools` package over the range -100 to 100 km s^{-1}.

We quantify the correctness of solutions using two metrics: the rms error (RMSE), which reflects the accuracy of the point estimates, and the rms standardized error (RMSSE), which reflects the accuracy of the uncertainty estimates. The expression for the RMSE is

$$\text{RMSE} = \left(\frac{1}{K} \sum_{k=1}^{K} (\log_{10} N_k - \log_{10} N_{\rm inp})^2 \right)^{1/2}, \quad \text{(B1)}$$

where k is an index over K replications of a particular test problem, $\log_{10} N_k$ is the mean of the posterior probability distribution over $\log_{10}$ total column density for problem k, and $\log_{10} N_{{\rm inp},k}$ is the input $\log_{10}$ total column density for problem k. The expression for the RMSSE is

$$\text{RMSSE} = \left(\frac{1}{K} \sum_{k=1}^{K} \left(\frac{\log_{10} N_k - \log_{10} N_{{\rm inp},k}}{\sigma_k} \right)^2 \right)^{1/2}, \quad \text{(B2)}$$

where σ_k is the estimated standard deviation of $\log_{10} N_k$. For well-calibrated σ_k and Gaussian-like posterior probability distributions, the RMSSE should be close to 1. Underestimated and overestimated σ_k will give RMSSEs above and below 1, respectively.

The first ground truth structure we test is MW foreground Fe II toward the star Sk 108 in the SMC (Welty et al. 1997). The absorption system consists of nine components with velocity centroids spanning 64 km s^{-1}, individual component b-parameters between 2.5 and 4 km s^{-1}, and a total column density of 6×10^{14} cm^{-2}. We generate 30 artificial spectra with this structure for CPRs of 10 and 30 and estimate total column densities using FOD, single Voigt profile fitting, and AOD done using the 1142, 1143, and 1144 Fe II lines. AOD has a high RMSE with any of these lines, being biased due to saturation for the 1143 and 1144 lines and being dominated by noise for the weaker 1142 line. FOD and single Voigt profile fitting have similar RMSEs of about 0.1 dex, but FOD has an RMSSE of 1.0 while Voigt profile fitting has an RMSSE of 1.4.

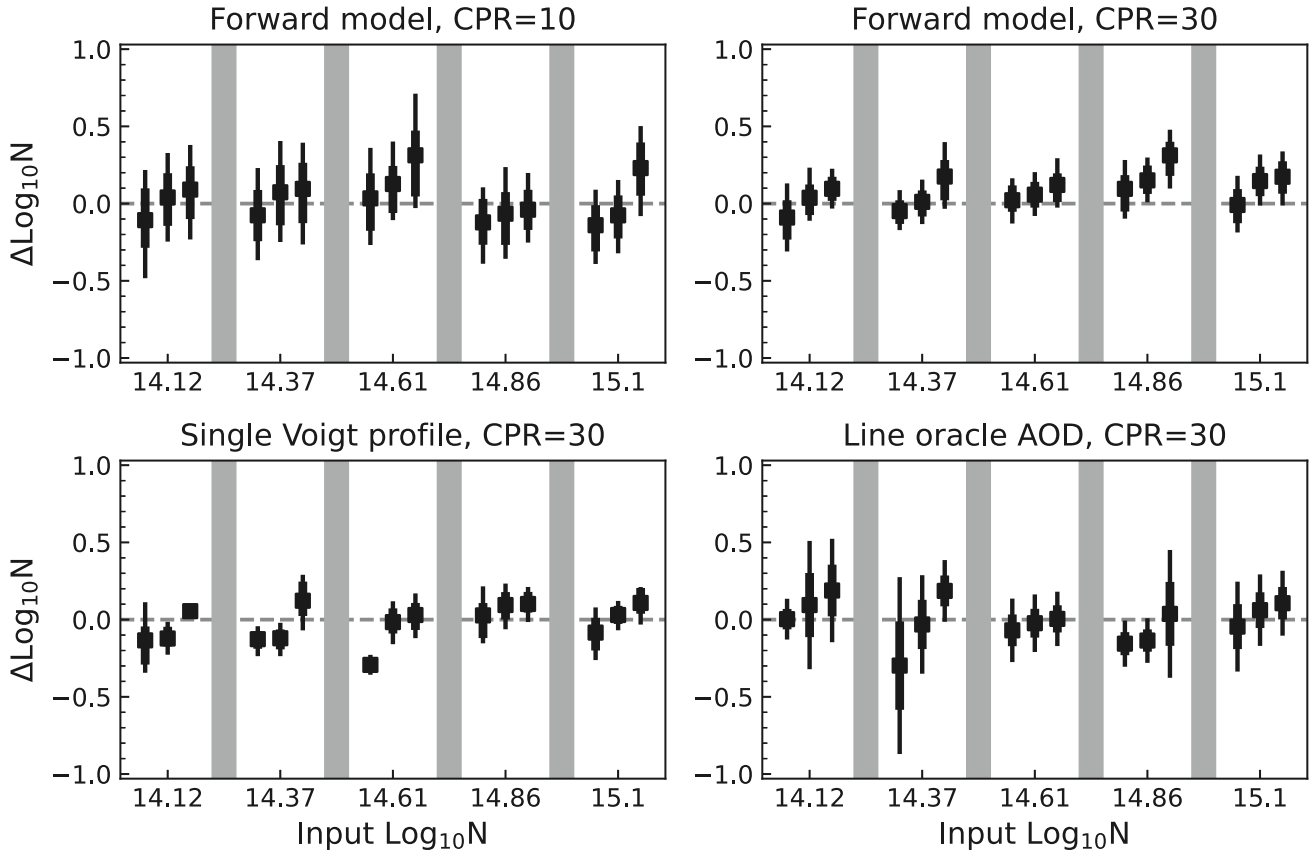

Figure 16. Results of estimating the column density of an injected single-component Fe II absorber using different methods. Panels corresponds to different solution methods or continuum photon count rates. Each panel shows log column density residuals (recovered value minus true value) as a function of true, input, column densities. For each input column density, we show the results of analyzing three spectrum realizations (i.e., three draws of a spectrum with the same input absorption profile but with different photon noise). Sets of results are separated by vertical gray bars. See Appendix B for a complete description of these tests.

Adding a second Voigt profile component does not improve the RMSSE and is not favored by frequentist or Bayesian model comparison methods. For the frequentist method, we find maximum likelihood solutions with one and two Voigt profile components and use the likelihood ratio test assuming a chi-squared distribution with three degrees of freedom for the test statistic sampling distribution. For the Bayesian method, we use product space MCMC (Carlin & Chib 2018) to calculate the Bayes factor for a two-component model relative to a single-component model. We apply these methods to the CPR = 30 spectra and find that none of the 30 artificial spectra show strong evidence (likelihood ratio test statistic in excess of 95%, Bayes factor greater than 10) in favor of a second component.

The second ground truth structure is a single Voigt profile at column densities spanning the range seen in the observations. The profile has a broadening parameter of 10 km s^{-1}, a centroid of 0 km s^{-1}, and input column densities ranging from $10^{14.12}$ to $10^{15.1}$ cm^{-2}, for Fe II, and from $10^{14.8}$ to $10^{15.8}$ cm^{-2}, for S II. The synthetic spectra cover the 1142 Å, 1143 Å, and 1144 Å lines, for Fe II, and the 1250 Å and 1253 Å lines for S II. This set of lines for S II reflects the coverage that is available for the Sextans A sight lines, where the stronger 1257 Å line is redshifted into much stronger MW Si II absorption.

We generate three artificial observations for each combination of the input total column density and CPR and measure column densities using FOD, MCMC Voigt profile fitting, and AOD. For AOD, we consider line-by-line measurements as well as a "line oracle" case, where the adopted measurement is the one that is closest to the truth. This is the *oracle* version because it is as though an oracle told the investigator which line was least affected by noise and saturation.

Figure 16 shows residuals as a function of true column density for the Fe II tests. All of the single-line AOD results have high RMSEs for some part of the true column density range. FOD, fitting a single Voigt profile, and line oracle AOD provide point estimates with RMSEs of 0.1–0.2 (depending on CPR). FOD and line oracle AOD also provide accurate estimates of the uncertainty on the point estimates, with RMSSEs of 1.0, while the single Voigt profile fits have underestimated uncertainties, with an RMSSE of 2.0.

Figure 17 shows residuals for the S II tests. At the highest true column densities, both S II lines are saturated. As a result, even the line oracle AOD produces results that are biased low. The posterior probability distributions from FOD and Voigt profile fitting are skewed to high values, with the FOD probability distributions being wider. This greater width is reflected in the RMSSEs: 1.1 for FOD and 1.4 for Voigt profile fitting.

FOD and Voigt profile point estimates for the total column have similar accuracy across both sets of tests, but FOD also produces well-calibrated uncertainties while Voigt profile fitting underestimates them. Line oracle AOD suggests a qualitative explanation for the performance of FOD. Forward modeling of the optical depth distribution accounting for the

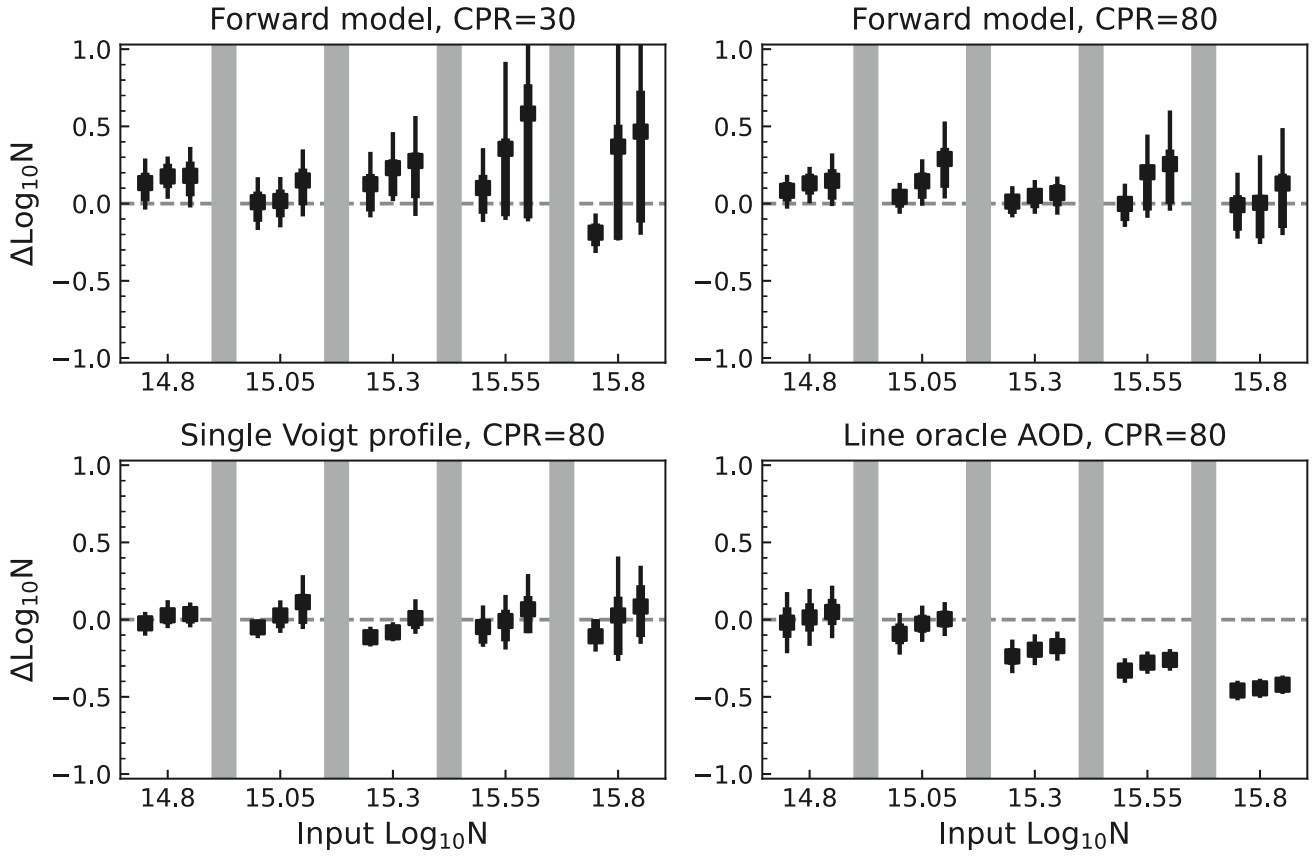

Figure 17. Results of estimating the column density of an injected single-component S II absorber using different methods. See Figure 16 for a description of figure elements.

instrumental LSF allows the method to "detect" if any of the available absorption lines are in the informative regime. If there are any, FOD performs similarly to line oracle AOD. If not, the flexibility of the model allows the uncertainties to (correctly) blow up.

ORCID iDs

Aleksandra Hamanowicz https://orcid.org/0000-0002-4646-7509
Kirill Tchernyshyov https://orcid.org/0000-0003-0789-9939
Julia Roman-Duval https://orcid.org/0000-0001-6326-7069
Edward B. Jenkins https://orcid.org/0000-0003-1892-4423
Marc Rafelski https://orcid.org/0000-0002-9946-4731
Karl D. Gordon https://orcid.org/0000-0001-5340-6774
Yong Zheng https://orcid.org/0000-0003-4158-5116
Miriam Garcia https://orcid.org/0000-0003-0316-1208
Jessica Werk https://orcid.org/0000-0002-0355-0134

References

Asano, R. S., Takeuchi, T. T., Hirashita, H., & Nozawa, T. 2013, MNRAS, 432, 637
Bigiel, F., Leroy, A., Walter, F., et al. 2008, AJ, 136, 2846
Bolatto, A. D., Leroy, A. K., Jameson, K., et al. 2011, ApJ, 741, 12
Bouret, J. C., Lanz, T., Hillier, D. J., et al. 2015, MNRAS, 449, 1545
Bresolin, F., Urbaneja, M. A., Gieren, W., Pietrzyński, G., & Kudritzki, R.-P. 2007, ApJ, 671, 2028
Camacho, I., Garcia, M., Herrero, A., & Simón-Díaz, S. 2016, A&A, 585, A82
Carlin, B. P., & Chib, S. 2018, J. R. Stat. Soc. B: Stat. Methodol., 57, 473
Chiang, I.-D., Sandstrom, K. M., Chastenet, J., et al. 2018, ApJ, 865, 117
Choudhuri, S., & Roy, N. 2019, MNRAS, 483, 3437
Clark, C. J. R., De Vis, P., Baes, M., et al. 2019, MNRAS, 489, 5256
Clark, C. J. R., Roman-Duval, J. C., Gordon, K. D., et al. 2023, ApJ, 946, 42
De Cia, A., Ledoux, C., Mattsson, L., et al. 2016, A&A, 596, A97
De Vis, P., Jones, A., Viaene, S., et al. 2019, A&A, 623, A5
Demyk, K., Meny, C., Leroux, H., et al. 2017a, A&A, 606, A50
Demyk, K., Meny, C., Leroux, H., et al. 2017b, A&A, 606, A50
Demyk, K., Meny, C., Lu, X. H., et al. 2017c, A&A, 600, A123
Diplas, A., & Savage, B. D. 1994, ApJS, 93, 211
Eales, S., Smith, M. W. L., Auld, R., et al. 2012, ApJ, 761, 168
Feldmann, R. 2015, MNRAS, 449, 3274
Fritz, J., Gentile, G., Smith, M. W. L., et al. 2012, A&A, 546, A34
Galliano, F., Galametz, M., & Jones, A. P. 2018, ARA&A, 56, 673
Garcia, M., & Herrero, A. 2013, A&A, 551, A74
Garcia, M., Herrero, A., Najarro, F., Lennon, D. J., & Alejandro Urbaneja, M. 2014, ApJ, 788, 64
Garcia, M., Herrero, A., Vicente, B., et al. 2009, A&A, 502, 1015
Gordon, K. D., Clayton, G. C., Misselt, K. A., Landolt, A. U., & Wolff, M. J. 2003, ApJ, 594, 279
Hildebrand, R. H. 1983, QJRAS, 24, 267
Hirashita, H. 2000, PASJ, 52, 585
Hoffman, M. D., & Gelman, A. 2014, JMLR, 15, 1593, http://jmlr.org/papers/v15/hoffman14a.html
Hunter, D. A., Ficut-Vicas, D., Ashley, T., et al. 2012, AJ, 144, 134
Ishwaran, H., & Rao, J. S. 2005, AnSta, 33, 730
Jenkins, E. B. 1996, ApJ, 471, 292
Jenkins, E. B. 2009, ApJ, 700, 1299
Jenkins, E. B., & Wallerstein, G. 2017, ApJ, 838, 85
Johnson, C. I., Plesha, R., Jedrzejewski, R., Frazer, E., & Dashtamirova, D. 2021, Updated Flux Error Calculations for CalCOS, Instrument Science Report, COS 2021-03, STScI
Jones, A. P., Tielens, A. G. G. M., & Hollenbach, D. J. 1996, ApJ, 469, 740
Kaufer, A., Venn, K. A., Tolstoy, E., Pinte, C., & Kudritzki, R.-P. 2004, AJ, 127, 2723
Kisielius, R., Kulkarni, V. P., Ferland, G. J., Bogdanovich, P., & Lykins, M. L. 2014, ApJ, 780, 76
Kniazev, A. Y., Grebel, E. K., Pustilnik, S. A., Pramskij, A. G., & Zucker, D. B. 2005, AJ, 130, 1558

Lamperti, I., Saintonge, A., De Looze, I., et al. 2019, MNRAS, 489, 4389
Lampton, M., Margon, B., & Bowyer, S. 1976, ApJ, 208, 177
Lorenzo, M., Garcia, M., Najarro, F., et al. 2022, MNRAS, 516, 4164
Morton, D. C. 2003, ApJS, 149, 205
Nersesian, A., Xilouris, E. M., Bianchi, S., et al. 2019, A&A, 624, A80
Ott, J., Stilp, A. M., Warren, S. R., et al. 2012, AJ, 144, 123
Péroux, C., & Howk, J. C. 2020, ARA&A, 58, 363
Popping, G., & Péroux, C. 2022, MNRAS, 513, 1531
Quiret, S., Péroux, C., Zafar, T., et al. 2016, MNRAS, 458, 4074
Rafelski, M., Wolfe, A. M., Prochaska, J. X., Neeleman, M., & Mendez, A. J. 2012, ApJ, 755, 89
Relaño, M., De Looze, I., Kennicutt, R. C., et al. 2018, A&A, 613, A43
Rémy-Ruyer, A., Madden, S. C., Galliano, F., et al. 2014, A&A, 563, A31
Roman-Duval, J., Elliott, E., Aloisi, A., et al. 2013, COS/FUV Spatial and Spectral Resolution at the new Lifetime Position, Instrument Science Report, COS 2013-07, STScI
Roman-Duval, J., Gordon, K. D., Meixner, M., et al. 2014, ApJ, 797, 86
Roman-Duval, J., Jenkins, E. B., Tchernyshyov, K., et al. 2021, ApJ, 910, 95
Roman-Duval, J., Jenkins, E. B., Tchernyshyov, K., et al. 2022a, ApJ, 928, 90
Roman-Duval, J., Jenkins, E. B., Tchernyshyov, K., et al. 2022b, ApJ, 935, 105
Roman-Duval, J., Jenkins, E. B., Williams, B., et al. 2019, ApJ, 871, 151
Rowlands, K., Dunne, L., Dye, S., et al. 2014, MNRAS, 441, 1017
Rowlands, K., Dunne, L., Maddox, S., et al. 2012, MNRAS, 419, 2545
Savage, B. D., & Sembach, K. R. 1991, ApJ, 379, 245
Schruba, A., Leroy, A. K., Walter, F., et al. 2012, AJ, 143, 138
Sembach, K. R., & Savage, B. D. 1992, ApJS, 83, 147
Shi, Y., Armus, L., Helou, G., et al. 2014, Natur, 514, 335
Skillman, E. D., Kennicutt, R. C., & Hodge, P. W. 1989, ApJ, 347, 875
Smith, M. W. L., Eales, S. A., Gomez, H. L., et al. 2012, ApJ, 756, 40
Stepnik, B., Abergel, A., Bernard, J.-P., et al. 2003, A&A, 398, 551
Tamburro, D., Rix, H. W., Leroy, A. K., et al. 2009, AJ, 137, 4424
Tautvaišienė, G., Geisler, D., Wallerstein, G., et al. 2007, AJ, 134, 2318
Tchernyshyov, K., Meixner, M., Seale, J., et al. 2015, ApJ, 811, 78
Tramper, F., Sana, H., de Koter, A., Kaper, L., & Ramírez-Agudelo, O. H. 2014, A&A, 572, A36
Tumlinson, J., Shull, J. M., Rachford, B. L., et al. 2002, ApJ, 566, 857
Vehtari, A., Gelman, A., Simpson, D., Carpenter, B., & Bürkner, P.-C. 2021, BayAn, 16, 667
Wakker, B. P., & Mathis, J. S. 2000, ApJL, 544, L107
Welty, D. E., Lauroesch, J. T., Blades, J. C., Hobbs, L. M., & York, D. G. 1997, ApJ, 489, 672
Welty, D. E., Xue, R., & Wong, T. 2012, ApJ, 745, 173
Ysard, N., Jones, A. P., Demyk, K., Boutéraon, T., & Koehler, M. 2018, A&A, 617, A124
Zhukovska, S., Dobbs, C., Jenkins, E. B., & Klessen, R. S. 2016, ApJ, 831, 147